



Erfan Mashayekh

CFD-Modeling of Lab-scale Microwave Plasma Torch for Carbon Dioxide Dissociation

IPP 2023-09
Oktober 2023

Masterarbeit
theoretisch

CFD-Modellierung eines Mikrowellen-Plasmabrenners im Labormaßstab für die Dissoziation von Kohlendioxid

Erfan Mashayekh

2023/09

Diese Seite und die darauffolgende in der gedruckten Version entfernen; nur für die PDF-
Version

Remove this and the next page in the print-out; This page is for the pdf-version only

Diese Seite in der Druckversion entfernen.
Remove this page in the print version.



Lehrstuhl für Energiesysteme

Titel der Materarbeit: CFD-Modellierung eines Mikrowellen-Plasmabrenners
im Labormaßstab für die Dissoziation von Kohlendioxid

Title of Master's Thesis: CFD Modeling of a Lab-scale Microwave Plasma Torch
for Carbon Dioxide Dissociation

Autor: Mashayekh, Erfan

Matrikelnummer: 03736829

Betreuer: Bastek, Sebastian, M.Sc.
Wilhelm, Sebastian, M.Sc.
Kiefer, Christian K., M.Sc.

Themensteller: Prof. Dr.-Ing. Hartmut Spliethoff
Technische Universität München
Lehrstuhl für Energiesysteme
Boltzmannstr. 15
85748 Garching b. München

Ausgegeben: 06.09.2023

Abgegeben: 06.09.2023

I hereby declare that this thesis is entirely the result of my own work except where otherwise indicated. I have only used the resources given in the list of references.

September 6th, 2023

Erfan Mashayekh

Acknowledgments

With gratitude, I extend my appreciation to the exceptional individuals who have played a pivotal role in bringing this master's thesis to completion. First and foremost, I extend my profound thanks to my lovely wife, Niloofar, whose belief in my academic pursuits and endless encouragement have been the cornerstone of my journey. Additionally, I extend my sincere appreciation to Christian Kiefer, Sebastian Wilhelm, and Sebastian Bastek, my supervisors, for their guidance, insightful feedback, and support that have been invaluable. Their mentorship has not only shaped the trajectory of this research, but has also encouraged my growth as a scholar. Finally, I want to express my sincere appreciation for the constant support and encouragement from Mahan. His encouragement throughout this research journey has been invaluable. This thesis represents more than just an academic accomplishment; it stands as a power of collaboration. With heartfelt thanks and warm regards, I extend my gratitude to each of you for being part of this memorable journey.

Kurzfassung

In diesem Beitrag wird die Entwicklung eines CFD-Modells für einen Mikrowellenplasmareaktor im Labormaßstab zur CO_2 -Dissoziation vorgestellt. Das Modell konzentriert sich auf Informationen über die Temperaturverteilung unter verschiedenen Betriebsbedingungen und verwendet eine symmetriebasierte Geometrie für eine effiziente Berechnung. Für die Modellierung der Wirbelströmung wurden gekoppelte druckbasierte Algorithmen, praktikable k - ϵ - und Reynolds-Stress (RSM) gewählt. Um die CO_2 -Dissoziation zu berücksichtigen, werden dynamische Gaseigenschaften einbezogen, ohne Gleichungen für den Speziestransport oder die Reaktionskinetik zu berücksichtigen. Neuronale Netze werden verwendet, um dreidimensionale Oberflächen zu modellieren, die mit Gaseigenschaftsdaten bei verschiedenen Druck- und Temperaturbedingungen korrelieren. Obwohl das Modell bei 1000 mbar vernünftige Ergebnisse lieferte, waren die vorhergesagten Temperaturen bei 200 mbar höher als in den experimentellen Daten. Weitere Sensitivitätsanalysen zeigten, dass weder das Turbulenzmodell noch die axiale Wärmequelle diese Diskrepanzen erklären konnten. Es wird angenommen, dass der Fehler eher numerisch als physikalisch bedingt ist.

Schlagwörter: Plasma Wirbelnde Strömung Dynamische Gaseigenschaften Wärmequelle

Abstract

This thesis presents the development of a CFD model for a laboratory-scale microwave plasma reactor designed for CO₂ dissociation. The model focuses on information on the temperature distribution under various operational conditions, utilizing symmetry-based geometry for computational efficiency. Coupled pressure-based algorithm, realizable k- ϵ , and Reynolds Stress (RSM) turbulence models were selected to model swirling flow. To account for CO₂ dissociation, dynamic gas properties are incorporated, without including species transport equations or reaction kinetics. Neural networks are employed to model three-dimensional surfaces that correlate with gas properties data across varying pressure and temperature conditions. Although the model exhibited reasonable results at 1000 mbar, the temperatures were predicted to be higher than in the experimental data at 200 mbar. Further sensitivity analysis indicated that neither the turbulence model nor the axial heat source distribution could explain these discrepancies. It is postulated that the error is of a numerical rather than a physical nature.

Key words: Plasma Swirling Flow Dynamic Gas Properties Heat Source

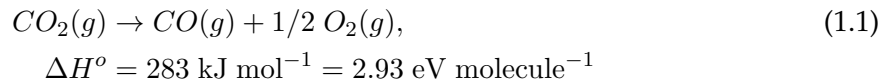
Contents

Acknowledgements	vii
Abstract	ix
1. Introduction	1
1.1. Motivation	1
1.2. Thesis Outline	3
2. Theory and Background	5
2.1. Conversion	5
2.2. Energy Efficiency	5
2.3. Background	6
3. Geometry and Grid	9
4. Governing Equations and Solvers	13
4.1. Flow Compressibility	13
4.2. Conservation Equations	14
4.3. Solver	16
5. Heat Transfer and Chemical Equilibrium	19
5.1. Thermodynamic and Transport Properties	19
5.1.1. Density and Molecular mass	20
5.1.2. Specific Heat Capacity	22
5.1.3. Thermal Conductivity	23
5.1.4. Dynamic Viscosity	25
5.2. Fluid Properties Fitting for Fluent	25
5.3. Volumetric Heat Source	28
5.3.1. Heat Source Distribution in Radial Direction	29
5.3.2. Heat Source Distribution in Axial Direction	30
6. Turbulence Model	33
6.1. Reynolds Stress	36
6.1.1. RNG k - ϵ Model	36
6.1.2. SST k - ω Model	37
6.1.3. RSM Model	37

6.1.4. Realizable k- ϵ Model	38
6.2. Turbulence Models Comparison	38
7. Boundary Conditions	41
7.1. Inlet	41
7.2. Outlet	41
7.3. Wall	41
7.4. Periodic Boundary	44
8. Results and Conclusion	47
8.1. Mesh Independence Study	47
8.2. Results at 1000 mbar	48
8.3. Temperature Profile at 200 mbar	49
8.4. Sensitivity Analysis	51
8.4.1. Effect of Turbulence Model	51
8.4.2. Effect of Heat Source	52
8.4.3. Velocity Profile Analysis	53
8.5. Conclusion	53
Appendix	59
A. UDF Sample Code	59
Bibliography	65

1. Introduction

Despite global efforts, the world continues to witness an annual release of more than 30 billion tonnes of carbon dioxide (CO₂) from fossil fuel combustion. This concerning trend reached a historic peak in 2021, with CO₂ emissions exceeding 37.12 billion tonnes [1]. The adoption of carbon capture, utilization, and sequestration (CCUS) for CO₂ is gaining popularity in order to align with the objectives of the Paris Agreement. The concept of CO₂ conversion takes on relevance within this paradigm, representing the transformation of CO₂ into valuable substances such as chemicals, fuels, or useful materials. The under investigation is known as CO₂ dissociation, which involves a chemical transformation of CO₂ into carbon monoxide (CO) and oxygen (O). The reaction that represents this process is as follows, where ΔH° represents the standard change in the enthalpy of the pure CO₂ splitting.



To gain an understanding of chemical reactions, Figure 1.1 shows the molar fractions of CO₂, CO, O₂, O and C as a function of temperature when a pure gas CO₂ is heated under atmospheric conditions obtained by the CEA program [2]. Chapter 5 offers a detailed explanation of the application and rationale of employing the CEA program.

There are several technologies for CO₂ conversion, including thermal, electrochemical, solar thermochemical, photochemical, biochemical, catalytic, and plasma. Among these, plasma technology differs in its exceptional flexibility, low investment costs, and scalability [3]. There are various types of plasma reactors, such as dielectric barrier discharges (DBD) [4], microwave (MW) discharges [5], glide arc (GA) discharges [6], and others. DBDs are non-thermal plasmas that operate around room temperature, whereas MW and GA discharges are warm plasmas that operate at gas temperatures around 6000 K. MW plasma torch is what is examined in this study and its general features are shown in Figure 1.2.

1.1. Motivation

The assessment of the dissociation process is based on understanding two metrics: energy efficiency and conversion rate. They will receive explanations in the subsequent sections (2.1 and 2.2). The achievement of a maximum dissociation process involves finding a connection between these parameters and the reactor temperature. Figure 1.3 illustrates

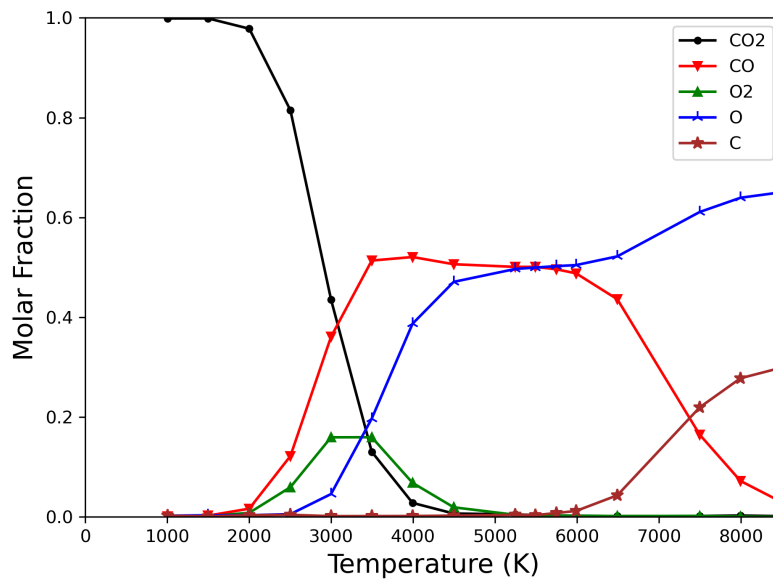


Figure 1.1.: The mole fraction of gases at atmospheric pressure to a given temperature at the calculated marked points using CEA.

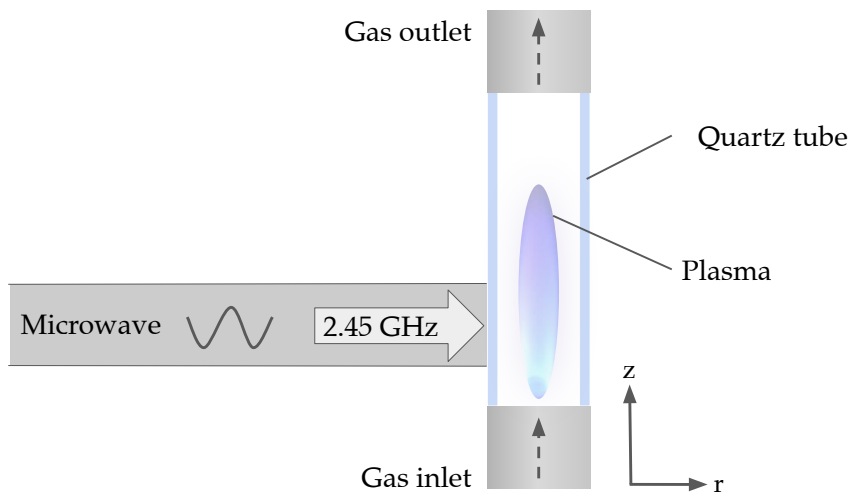


Figure 1.2.: General features of a microwave discharge.

the interaction between theoretical thermal conversion and the corresponding energy efficiency with respect to temperature in the CO₂ dissociation process [3]. The motivation for this thesis is to acquire detailed temperature information because it plays a crucial role in conducting a comprehensive analysis of conversion and energy efficiency. To achieve this goal, the thesis aims to utilize CFD to create a numerical model. This model will enable the prediction of fluid behavior, with a particular focus on understanding how temperature is distributed within the plasma reactor.

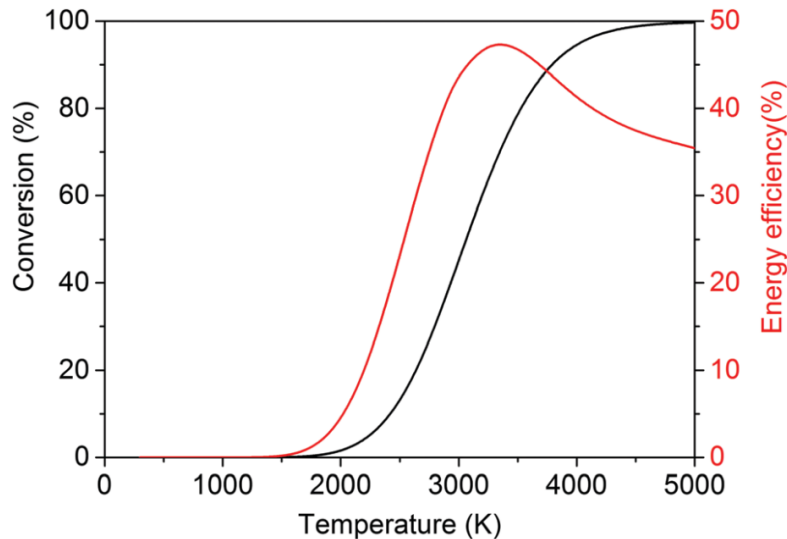


Figure 1.3.: Thermal conversion and energy efficiency for pure CO₂ dissociation [3]

1.2. Thesis Outline

Chapter 2 elaborates more on the motivation of the thesis to determine the temperature distribution within the reactor by providing background information.

Accurate representation of the plasma torch geometry is crucial for faithful simulations. In addition, the generation of an appropriate computational grid is essential to obtain reliable and efficient results. Chapter 3 elaborates on the methodologies used to construct the geometry of the laboratory-scale reactor and the grid generation process. The reasoning behind these choices is thoroughly explained, highlighting their impact on the accuracy of the numerical model.

The governing equations form the backbone of any CFD simulation. The choice of appropriate governing equations depends on the specific characteristics of the problem at hand. Chapter 4 elucidates the thesis rationale for selecting the governing equations and the related solver.

In addition to the fundamental considerations of governing equations, accounting for chemical equilibrium and plasma-chemistry reactions is of paramount importance in simulating plasma torches accurately. Plasma involves complex interactions between different species and chemical reactions, which significantly influence the overall behavior and characteristics of plasma. However, to reduce complexity and enhance computational efficiency, this study utilizes a model that circumvents the inclusion of reaction kinetics equations and multiple species physics. Instead, it adopts a strategy involving dynamic gas properties and an additional source term to emulate the same underlying physics. This approach proves to be less complicated, which is introduced in 5.

Turbulence, an inherent feature of many fluid flows, poses challenges for numerical simulations. Turbulence models play a crucial role in capturing the intricate interactions and fluctuations that occur in turbulent flows. Chapter 6 delves into the considered turbulence modeling approaches and the rationale behind the selection of the most suitable model for plasma simulation.

Boundary conditions are one of the aspects of numerical solvers and affect the accuracy and reliability of the results. Chapter 7 underscores the importance of properly defining boundary conditions, particularly in the context of plasma simulations. This study explores the effects of boundary conditions on near-wall turbulence and elucidates the importance of accurate inlet and outlet boundary conditions. Moreover, this chapter elucidates an approach that is used to model the presence of an air-cooling system located in proximity to the reactor walls.

Chapter 8 delves into an analysis of temperature distribution results in different operating conditions, offering a detailed exploration of the observed differences.

For the simulations, this study has chosen to utilize ANSYS Fluent software due to its proven track record of reliability, robust capabilities, and comprehensive features [7]. ANSYS Fluent has established itself as a trusted and widely recognized tool in the field of fluid dynamics simulations, renowned for its accuracy and efficiency in capturing complex fluid behaviors.

2. Theory and Background

This chapter introduces key performance metrics, conversion and energy efficiency, and provides further insights into the study's motivations.

2.1. Conversion

In general, conversion can be defined in absolute or effective form based on the literature. The absolute version is of interest in this study which is explained by Snoeckx *et al.* [3] as follows:

$$\chi_{CO_2} = 1 - \frac{\dot{n}_{CO_2,out}}{\dot{n}_{CO_2,in}} \quad (2.1)$$

In this context, the quantities $\dot{n}_{CO_2,in}$ and $\dot{n}_{CO_2,out}$ correspond to the molar flows of CO₂ at the inlet and exhaust of the reactor, respectively.

2.2. Energy Efficiency

Prior to establishing the definition of energy efficiency, it is imperative to recognize the importance of Specific Energy Input (SEI) as a pivotal element in the analysis of energy efficiency and conversion in a plasma process. SEI is quantified as the ratio of plasma power to the rate of gas flow at the inlet [3]. SEI in terms of watts (W) and standard liters per minute (slm) is defined as follows [8]:

$$SEI = \frac{0.0139 \text{ Power [W]}}{\text{Flowrate [slm]}} \quad (2.2)$$

The standard flow rate here is considered at the standard temperature of 0 °C and standard pressure of 101 325 Pa. Based on the specific energy input, energy efficiency is an indicator of how effectively the process occurs in comparison to the standard reaction enthalpy [3] and is defined as follows:

$$\eta = \frac{\chi_{CO_2} \Delta H^o}{SEI} = \frac{\chi_{CO_2} \Delta H^o \text{ Flowrate [slm]}}{0.0139 \text{ Power [W]}} \quad (2.3)$$

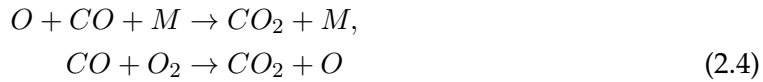
ΔH^o , as previously expressed in Equation 1.1, is the standard enthalpy of the dissociation reaction of CO₂.

2.3. Background

As elaborated in Chapter 1, the main objective of the CO₂ dissociation process is to achieve notable levels of conversion and energy efficiency. Among the variety of plasma reactor configurations, the microwave plasma reactor has emerged as the best in achieving conversion rates and energy efficiency values in a pressure range of 1 to 1000 mbar [3]. In this study, the microwave plasma torch is used to be the type of microwave discharge for simulations.

According to literature, plasma within this pressure range exhibits two distinguishable modes: diffusive mode and contracted mode. The diffusive mode, observed at pressures below 100 mbar, results in gas temperatures reaching around. An increase in pressure forces the plasma to contract, elevating the gas temperatures to approximately 6000 K at its core 3000 K [9, 10]. The contracted plasma mode was chosen for this study. As a result, the attention of this study has been drawn to pressure ranges ranging from 200 mbar to 1000 mbar in all simulations.

Thermal dissociation is limited by two main constraints. When using a simplified thermal equilibrium model of CO₂ gas is used, the possible energy efficiency is limited to around 50 % at 3000 K and around 30 % at 6000 K [9]. In addition, conversion is limited by the presence of recombination reactions in the effluent.



Research investigations have revealed that fast cooling of the effluent can serve as an effective strategy to mitigate the effects of recombination [5]. To realize and improve the fast cooling approach, Kiefer *et al.* [11, 12] and Hecimovic *et al.* [8, 13] conducted experimental studies on the reactor. To gain insight from these studies, three primary configurations are illustrated in Figure 2.1.

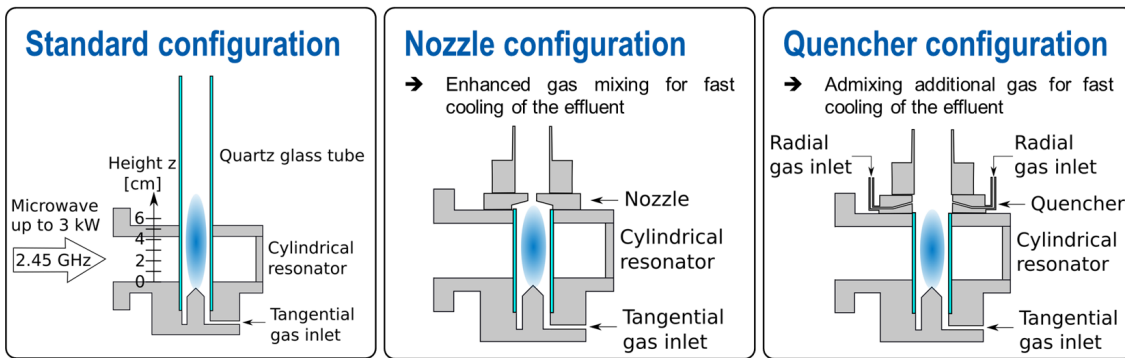


Figure 2.1.: Different configuration of the plasma reactor [12]

The first configuration represents the standard setup, devoid of any extensions downstream of the plasma torch, as depicted in figure 2.1. However, to address the fast cooling

technique, two additional configurations involving a nozzle and a quencher were explored within laboratory settings. The former configuration improves the gas mixing to facilitate rapid cooling of the effluent, while the latter introduces supplementary gas for rapid cooling [11, 12, 8, 13]. These studies have shown that by using a nozzle or quencher, a significant increase in both conversion and energy efficiency is obtained. However, there is still an opportunity to improve the design towards higher values. The overall goal is to enhance the quenching rate. Therefore, a target design can enhance gas turbulence for better mixing and increase the cooled gas surface area. In such a state, simulation can help to achieve a better understanding of the flow behavior, especially the temperature distribution and turbulence inside the reactor. Understanding the temperature is the key to determining the molar flow of species within the reactor. Having a grasp of the molar flows enables the application of equations 2.1 to 2.3 to derive reactor conversion and energy efficiency. Although finding the molar fractions and calculating the conversion and efficiency are not in the scope of this thesis, it was necessary to highlight the relation of temperature with these parameters.

As a result, the aim of this study is to employ the most relevant numerical tools to simulate the flow dynamics, particularly the temperature distribution within the reactor, while tailoring them to suit this study case. The investigation exclusively centers on simulating plasma in configurations that lack cooling elements such as quenchers or nozzles. For simulations, the geometry of the quencher configuration examined by Kiefer et al. is adopted, with the omission of secondary cooling inlet flows [11].

3. Geometry and Grid

Building on the insights provided in Chapter 2 on reactor configuration, this thesis investigates flow dynamics particular to the 'Quencher' shape with the exception that cooling flow components are not included. Figure 3.1 provides a complete visual picture of the overall structure of the reactor.

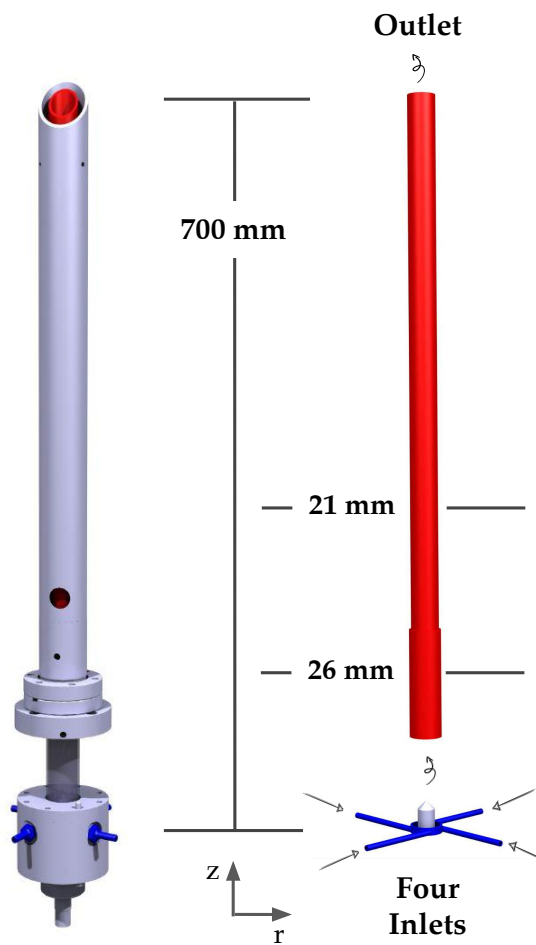


Figure 3.1.: Exploring the CATIA V5 model: Reactor structure (left) and gas flow path (right)

3. Geometry and Grid

As shown in the diagram, the CO₂ gas enters the reactor through four inlet tubes with diameters of 4 mm. These tubes are tangentially attached to the lower part of the reactor. The gas, moving in a swirling motion, traverses the resonator and ascends toward the quartz tube, which measures 80 mm in length and 26 mm in inner diameter. This precise zone is where plasma is generated. The temperature of the gas increases, causing CO₂ to dissociate into a variety of gases and charged particles. Then, this gas mixture is transmitted towards the exhaust while maintaining its swirling motion. It should be noted that the diameter of the exhaust tube has been reduced to 21 mm. The change meets a specific purpose: A second tube with larger diameter surrounds this tube with the cooling water flow in between. This configuration, which is also known as a double-pipe heat exchanger, efficiently reduces the temperature of the surrounding wall. Figure 3.2 shows the geometry that acts as the main focus of the simulation, showing the proportions of various components of the reactor.

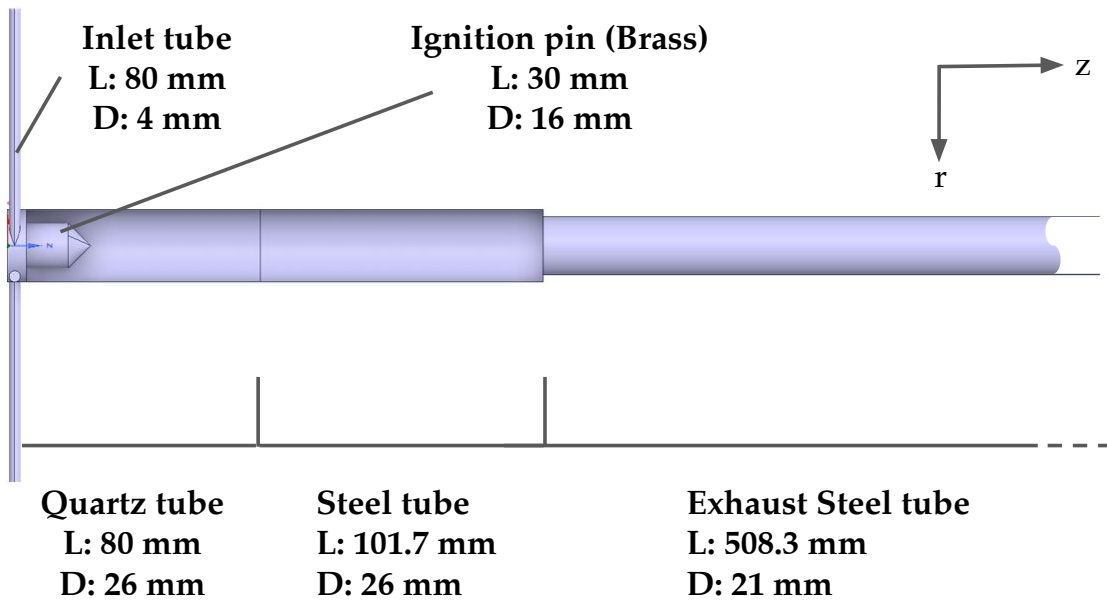


Figure 3.2.: The size of different parts in the reactor as implemented in the CFD model. "L" and "D" represent length and diameter respectively.

To optimize computational efficiency, only a quarter of the model is simulated, as seen in Figure 3.3. Using a rotational symmetry boundary condition in CFD simulations could result in significant time savings, often exceeding 50%. Another advantage is the possibility of using extra memory to perform more precise simulations. This can involve using a higher density of mesh cells concentrated in specific areas of interest. Following the geometry of the model shown in Figure 3.3, taking advantage of this opportunity, it is divided

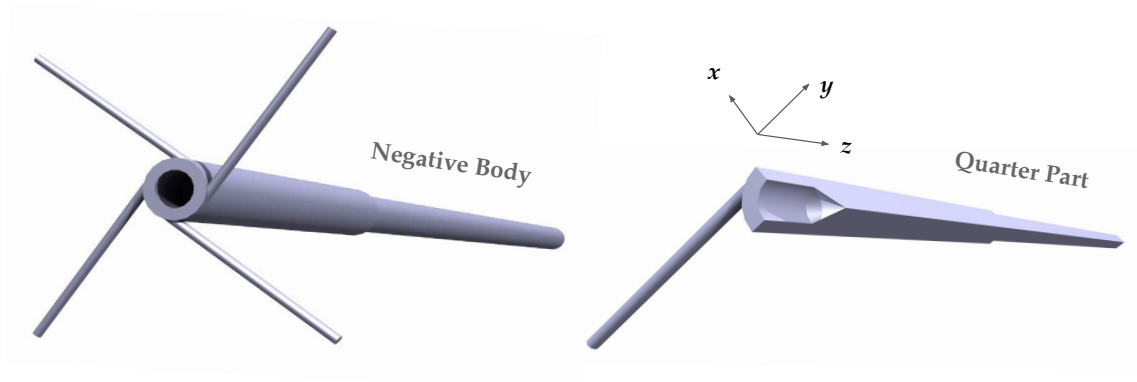


Figure 3.3.: Three-dimensional model. Left: Geometry of the model . Right: Quarter of the geometry.

into four separate pieces and solves only the equations for one piece. Two surfaces are created that are at right angles to each other. In this scenario, the slicing procedure yields two surfaces, which are treated as periodic boundary conditions. This means that whatever occurs on one surface is linked to the other in a continuous loop. Chapter 7 explains further details of how these boundary conditions are applied.

In this study, six grids were created for simulations, covering a range of large to fine grids. To facilitate this grid study, the six grids shared the same basic structure. The domain was divided into three main segments according to the axial length, as shown in Figure 3.4. Starting from the region with the smallest cell size, "X," the other regions contained cells with sizes "2X" and "4X," respectively. Table 3.1 provides essential information for each grid, specifying the cell size for each of the three parts and the total number of cells in each grid.

3. Geometry and Grid

Part	1	2	3
Cell Size	X	2X	4X
Axial Length (mm)	0 - 160	160 - 220	220 - 700

Figure 3.4.: Grid with three main cell sizes based on the axial length.

Grid ID	Cell Size (mm)			Number of Cells
	Part 1	Part 2	Part 3	
1	0.62	1.25	2.5	113151
2	0.50	1.00	2.00	205062
3	0.39	0.79	1.58	375347
4	0.31	0.62	1.25	687087
5	0.25	0.50	1.00	1307020
6	0.20	0.39	0.79	2436849

Table 3.1.: Number of cells at each grid.

4. Governing Equations and Solvers

Before delving into the mathematical equations governing the simulation, two fundamental questions need to be considered. First, the choice must be made between solving for steady-state or transient conditions must be made. Second, an assessment of whether the system's flow can be simplified as incompressible or the inclusion of compressibility effects is necessary.

The answers to these questions are critical because they help to find the most appropriate equations for a unique study. Notably, many experimental techniques involve measuring properties averaged over time, which implies a time-averaged behavior. Given this, the final solution and the obtaining of a steady state condition for the equations are of importance. However, the question of fluid compressibility remains unresolved and deserves further exploration. To find this out, the following part looks at compressibility.

4.1. Flow Compressibility

Table 4.1 provides an overview of the gas flow rate range simulated under various operating pressures in this study. Although the simulations cover more pressure conditions in the range between 200 and 1000 mbar, the specific 20 slm gas flow rate at 200 mbar corresponds to the highest velocity in the simulations, directly determining the compressibility of the flow due to velocity, since a flow is considered incompressible if its Mach number is lower than 0.3 [14]. Equation 4.1 represents the Mach number. This value is obtained by dividing the magnitude of the velocity vector \vec{u} by the speed of sound. It is a crucial parameter that helps to understand how fast the flow is moving compared to the speed at which sound travels through the medium.

$$M = \frac{|\vec{u}|}{a} \quad (4.1)$$

After examining the maximum achievable speed within the four tubes supplying the reactor, each having a width of 4 mm, an interesting observation emerges. The initial speed within these tubes is significantly lower than 40 m/s, suggesting that it falls well below the speed of sound. The approach of calculating the velocity from the standard flow rate can be found in Section 7.1. Overall, this concept is further emphasized when examining the data in Table 4.2, which illustrates an extreme scenario with the highest attainable speed at a temperature of 300 K. Even if the velocity doubled hypothetically, the resulting Mach number would still remain well below 0.3, which is the critical threshold. In essence, the flow through the tubes remains incompressible.

Pressure (mbar)	Gas Flow Rate (slm)
200	5 - 20
1000	10 - 50

Table 4.1.: Operating conditions of interest in this study

Pressure (mbar)	200
Flowrate (slm)	20
Velocity (m/s)	40
Speed of sound (m/s)	270.15
Mach number	$0.137 < 0.3$

Table 4.2.: Mach number estimation for the inlet flow at 300 K.

The simulation in this study does not include simulating flows when compressibility is important. As a result, density-based solutions designed expressly for such compressible flows are irrelevant here. Further details on the different types of solvers can be found in 4.3.

It is critical to recognize that flow models with a nozzle, as shown by Hecimovic *et al.* [8], show the appearance of high-speed, sometimes even supersonic flows near the nozzle. As a result, a density-based solver becomes more relevant in scenarios involving such compressible flow patterns. This is because the Mach number exceeds 0.3, which signals the need for specialized consideration of compressibility effects, especially the changes needed in the energy equation due to pressure work and kinetic energy.

4.2. Conservation Equations

As explained in the beginning of this chapter, the selection of steady-state equations is more of interest in the simulation approach. Furthermore, as detailed in the preceding section, the flow is considered incompressible because of its relatively low velocity. According to Chapter 1, the plasma temperature rises to 6000 K inside the reactor. This elevation in temperature directly impacts the density, causing it to decrease. Therefore, the term "incompressible" does not mean that the density remains constant within the reactor. The influence of compressibility becomes apparent in the energy equation, which will be discussed in the forthcoming explanation of the energy equation.

The steady-state continuity equation represents mass conservation within fluid flow

[14]. This equation is mathematically expressed as:

$$\nabla \cdot (\rho \vec{u}) = 0 \quad (4.2)$$

Here, ρ denotes the density, and \vec{u} is the velocity vector. The steady-state Navier-Stokes equations govern the conservation of momentum in an inertial (non-accelerating) reference frame, as described in [15]. They capture the interaction between pressure gradients and viscous forces, allowing for a thorough examination of the motion of the fluid. The steady-state Navier-Stokes equations without any external forces and the buoyancy effects are expressed as follows.

$$\nabla \cdot (\rho \vec{u} \vec{u}) = -\nabla p + \nabla \cdot \bar{\bar{\tau}} \quad (4.3)$$

p represents the pressure, $\bar{\bar{\tau}}$ denotes the stress tensor which is described below.

$$\bar{\bar{\tau}} = \mu \left[(\nabla \vec{u} + (\nabla \vec{u})^T) - \frac{2}{3} \nabla \cdot \vec{u} \bar{\bar{I}} \right] \quad (4.4)$$

Here, μ denotes the dynamic viscosity, and $\bar{\bar{I}}$ is the unit tensor. In addition to the Navier-Stokes equations, the energy equation is incorporated into the simulation setup to analyze the temperature distribution and thermal behavior within the plasma torch. This equation accounts for both conduction and convection mechanisms, offering insights into the heat transfer within the plasma under steady-state conditions. The steady-state energy equation is expressed as [16]:

$$\nabla \cdot (\rho \vec{u} e) = -\nabla \cdot q + P_v \quad (4.5)$$

Here, e is the specific internal energy, q denotes the heat flux, and P_v is the term of the heat source (W/m^3). Equation 4.5 considered the conservation of specific internal energy e . According to the Fourier law $q = -\kappa \nabla T$ where κ is thermal conductivity [16].

$$\nabla \cdot (\rho \vec{u} e) = \nabla \cdot (\kappa \nabla T) + P_v \quad (4.6)$$

Pressure-based algorithms solve Equation 4.6 in order to obtain temperature within the computational domain. However, the density-based algorithm solves an energy equation that assumes the conservation of total energy. The total energy is equal to the sum of internal and kinetic energy $E = e + K$. This leads to additional terms on both sides of the Equation 4.6 [16]. Ansys Fluent implements Equation 4.7 in the case of using density-based solvers.

$$\nabla \cdot (\vec{u}(\rho E + p)) = \nabla \cdot (\kappa \nabla T) + P_v + \nabla \cdot (\bar{\bar{\tau}} \cdot \vec{u}) + \rho g \cdot \vec{u} \quad (4.7)$$

where g denotes the standard acceleration due to gravity. The term on the left-hand side is a combination of pressure work $\nabla \cdot (p \vec{u})$ and the total energy convection term $\nabla \cdot (\rho \vec{u} E)$. Here, $\bar{\bar{\tau}}$ is the stress tensor and represents viscous heating. In Fluent, it is also possible to include the additional terms on the right-hand side of Equation 4.7 in pressure-based solvers.

4.3. Solver

In the endeavor to solve the set of Equations (4.2-4.7), the use of a robust and efficient solver is imperative. Traditionally, pressure-based solvers have been designed to simulate incompressible flows, while density-based solvers have been crafted to address compressible scenarios. However, in the most recent iterations of Ansys Fluent and other CFD platforms, both approaches have been refined to accommodate a wide spectrum of flow conditions. Guided by the insights provided in Sections 4.1 and 4.2, where the data indicate relatively low flow velocities, the inclusion of supplementary terms in the energy equation using density-based methods becomes redundant.

Although density-based solvers are more accurate, they often take longer to reach convergence. This happens because all three conservation equations are computed simultaneously in these solutions, adding complexity. Pressure-based solvers, on the other hand, speed up the process. In their coupling technique, they first focus on the momentum and Navier-Stokes equations, deferring the energy equation until later. This approach improves the computational efficiency of pressure-based solvers [17]. This consideration leads to favoring the use of pressure-based solvers for simulation, as their computational efficiency aligns better with the specific characteristics of this flow scenario in this study.

Within the simulation framework of this study, the coupled pressure-based algorithm is employed, a computational approach that effectively addresses a system of interconnected equations. This system involves the momentum equation and the continuity equation. The coupling approach helps to ensure consistency between the pressure and velocity distributions, leading to improved accuracy in capturing flow behaviors. This algorithm is described in Figure 4.1.

The first step of the algorithm involves updating the properties of the fluid. This includes scalar fields such as density, viscosity, specific heat, and thermal conductivity, all of which are adjusted on the basis of the current state of the solution. Chapter 5 explains how these properties can be obtained.

Once the fluid properties are acquired, a coupled solution to the momentum and continuity equations becomes attainable. This technique offers enhanced solution convergence and stability compared to segregated pressure-based algorithms [19]. Although this advancement proves beneficial, it is important to recognize that the memory demands of this method increase. This arises from the necessity of storing the discrete system of both equations within the memory while solving for the pressure and velocity fields. The next step is the adjustment of the mass fluxes.

The next step involves solving equations related to additional factors such as turbulence behavior, energy distribution, and substance concentration. It should be noted that for this study complex equations related to various species and chemical reactions are not included in the calculations. Further elaboration on this topic can be found in Chapter 5.

Approaching the final stage of the computational process, a critical task lies ahead: assessing convergence within the coupled pressure-based algorithm. This step confirms that the solution has not only converged but has also stabilized to a degree where additional

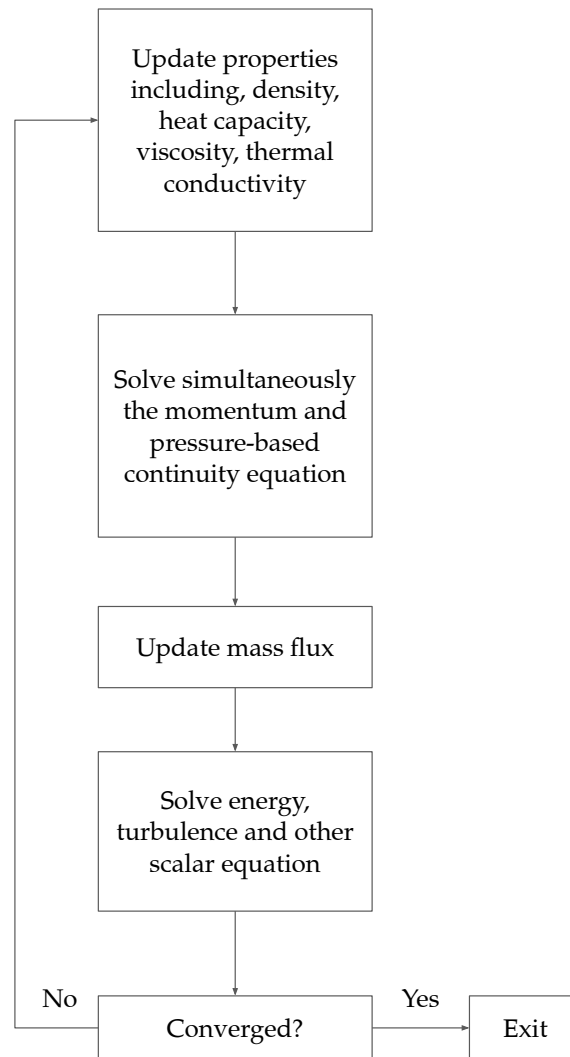


Figure 4.1.: Coupled pressure-based algorithm [18]

iterations would result in minimal changes.

For the purpose of the specific simulation approach, a convergence criterion has been defined. To assess the precision of the results, a threshold for residual values has been established. For the continuity equation, a residual of less than 1×10^{-3} is required, indicating the need to minimize changes in mass conservation. Furthermore, for the remaining equations, a lower threshold of 1×10^{-4} is set. Residual is defined by the sum of numerical errors, which means how much the variables change between two iterations. Beyond these residual criteria, the assessment extends to physical errors, providing information on the overall simulation performance. Specifically, parameters such as the average velocity at the outlet, the overall mass flow rate, and the overall energy-transfer fluxes are examined. These parameters must meet a threshold of less than 1×10^{-3} .

5. Heat Transfer and Chemical Equilibrium

The dissociation of CO_2 comprises many reactions as explained in Chapter 1. On the basis of Figure 1.1, at temperatures higher than 2000 K, reactions begin, which gradually change the transport and thermodynamic properties of the whole mixture. To avoid the burden of including numerous reaction equations, the approach developed by Brochet *et al.* [20] is used. Instead of explicitly incorporating individual chemical reactions and solving the conservation equations for each species separately, this approach introduces a gas mixture with dynamic properties in all conservation equations, helps to focus on a single representative species within the reactor.

The representative gas mixture chosen for the simulation plays a central role in the plasma dynamics and chemical processes. Its properties, including heat capacity, thermal conductivity, viscosity, molecular mass, and density, are essential parameters that govern its behavior under different temperature and pressure conditions. By solving the equations for a single species, while considering its dynamic properties, this study achieves a representation of the plasma torch's behavior without explicitly accounting for the multitude of reactions that take place. This approach significantly reduces computational complexity, making the simulation more computationally efficient while preserving the essential physics and chemistry involved. The following section will elaborate on the acquisition of these dynamic properties.

5.1. Thermodynamic and Transport Properties

As highlighted earlier, the approach involved the utilization of a representative gas mixture, characterized by its dynamic properties, within the framework of equations (4.2) to (4.6). In contrast to adopting fixed values for crucial parameters such as density, heat capacity, thermal conductivity, molecular mass, and dynamic viscosity, a different approach is implemented. These properties are incorporated as functions of temperature and pressure.

This method was implemented making use of the capabilities of the NASA-developed software program known as CEA (Chemical Equilibrium with Applications) [21]. This advanced program, CEA, proved instrumental in generating the property data required for the simulations. Through this program, this study acquired properties that vary over a wide range of temperatures, ranging from 200 to 11 500 K, and encompassing a pressure range of 200 to 1000 mbar. CEA is independent of space and time and uses thermodynamic models to compute the gas properties. These properties are characterized by the tempera-

ture and pressure values assigned in this study. Although the CEA computer program is used for property determination, it is worth providing a brief overview of the calculation process used by it.

5.1.1. Density and Molecular mass

Density changes due to pressure gradients are negligible, as discussed in Section 4.1. This phenomenon becomes evident primarily in the energy equations, where the influence of pressure work and kinetic energy is negligible. However, it is important to recognize that the density is not constant, especially in regions close to the plasma, where temperatures soar to almost 6000 K. This drastic temperature increase quickly lowers the density within these specific areas. With this understanding in mind, this section will elucidate the conservation equations.

As discussed in Section 4.3, the update of density is intimately linked to the pressure and temperature fields within the system. In this study, the determination of the density for the entire reactor is based on the application of the ideal gas law. Ansys Fluent employs the following equation to calculate density [18]:

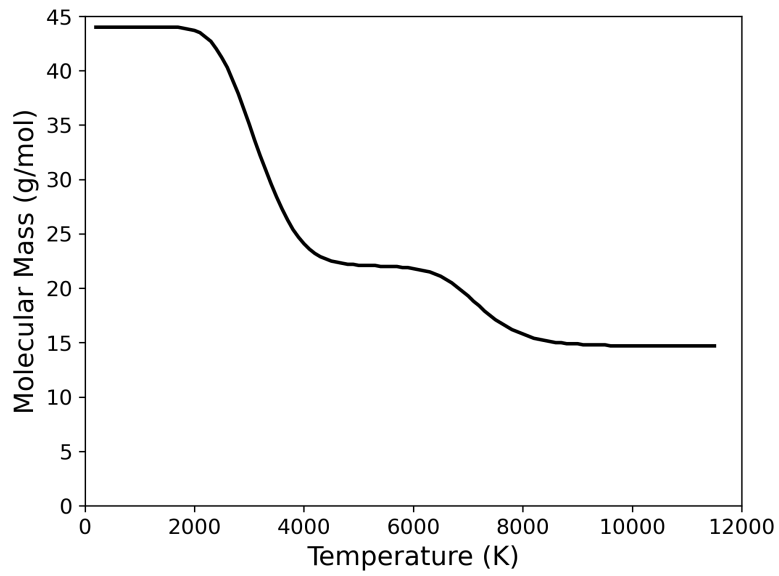
$$\rho = \frac{p}{\frac{R}{M}T} \quad (5.1)$$

Here, R corresponds to the universal gas constant ($8.314 \text{ J K}^{-1} \text{ mol}^{-1}$), and M represents the molecular mass of the mixture. The molecular mass (M) is determined by summation of the molar fractions and molecular mass of the individual species, as expressed in the following equation:

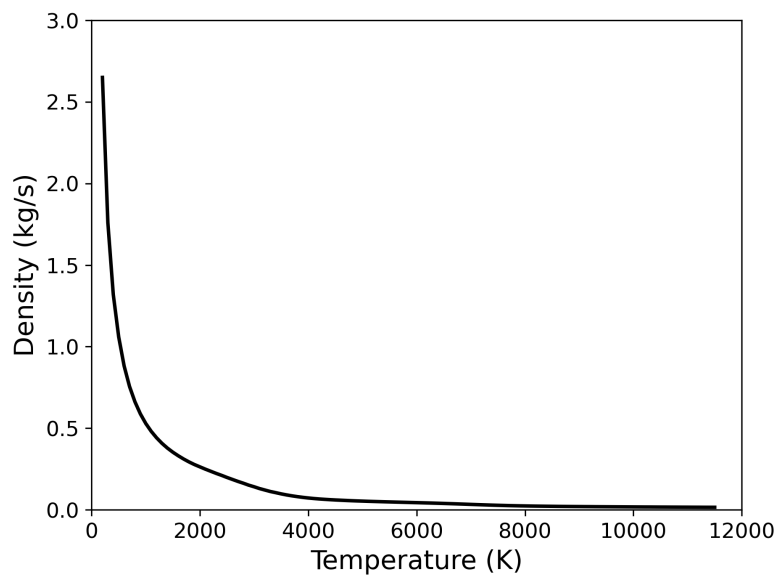
$$M = \sum_{i=1}^{\text{NS}} x_i M_i \quad (5.2)$$

In this equation, x_i denotes the molar fraction of species i , while M_i represents the molecular mass of species i . The term NS corresponds to the count of species within the mixture. Figure 5.1a shows the changes in effective molecular mass of the gas mixture for different temperatures.

It is important to note that when the ideal gas law is used to calculate the density in Ansys Fluent, the software assumes a constant molecular mass. To avoid this situation, Equation 5.1 can be used to calculate the density while accounting for the temperature variations. This variation in density may then be included into Fluent via a User-Defined Function (UDF), helping to represent the density as a function of temperature. Figure 5.1b represents the density based on temperature changes at a specified pressure of 1 bar. Furthermore, when opting for a user-defined density value in Fluent, it is essential to include the speed of sound as well. This is because the software assumes a departure from the ideal gas law. Although the speed of sound does not influence the solution, it is necessary



(a)



(b)

Figure 5.1.: Molecular mass and Density of the mixture at $p = 1000$ mbar

for auxiliary calculations. [18]. The speed of sound for an ideal gas is defined by

$$a = \sqrt{\gamma \frac{p}{\rho}} \quad (5.3)$$

γ is the adiabatic index and slightly changes with temperature alterations. Fortunately, CEA also provides the relations for a . Figure 5.2 depicts speed of sound for different temperature values at the pressure value of 1 bar.

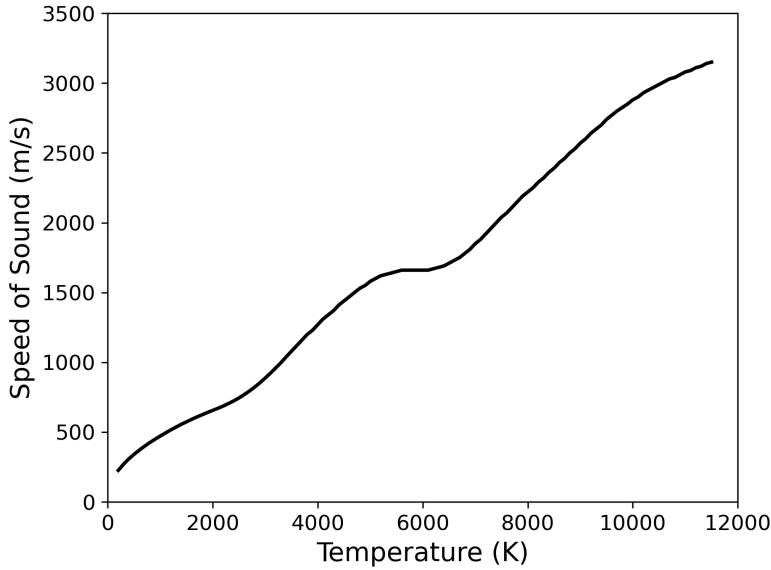


Figure 5.2.: Speed of sound at $p = 1000$ mbar

5.1.2. Specific Heat Capacity

In a general context, the concept of heat capacity can be characterized by expressing it as the first derivative of enthalpy with respect to temperature under conditions of constant pressure. This relationship can be denoted as $c_p \equiv (\partial h / \partial T)_p$. However, it is essential to recognize that this derivative is not a fixed value and can exhibit variations based on the specific thermodynamic processes at play. A notable consideration emerges when differentiating between scenarios in which the composition of the system reaches equilibrium rapidly or gradually over time. In the first case, this derivative is termed the "reaction" heat capacity, while in the latter scenario, where reaction processes evolve extremely slowly, it is termed the "frozen" heat capacity [21].

The equilibrium heat capacity ($c_{p,eq}$) is a composite value that includes both frozen and reaction contributions. The equilibrium heat capacity of a mixture can be expressed

through the summation of these contributions, encapsulating the specific heat capacity under reaction conditions as well as frozen conditions.

$$c_{p,eq} = c_{p,f} + c_{p,r} \quad (5.4)$$

Here, $c_{p,f}$ is defined by:

$$c_{p,f} = \sum_{j=1}^{NS} n_j C_{p,j}^o \quad (5.5)$$

$c_{p,r}$ is also defined by:

$$c_{p,r} = \sum_{j=1}^{NG} n_j \frac{H_j^o}{T} \left(\frac{\partial \ln n_j}{\partial \ln T} \right)_p + \sum_{j=NG+1}^{NS} \frac{H_j^o}{T} \left(\frac{\partial n_j}{\partial \ln T} \right)_p \quad (5.6)$$

H_j^o and $C_{p,j}^o$ represent the molar enthalpy and specific heat of species j under standard conditions at temperature T , respectively, while n_j represents the amount of kilogram-moles of species j per kilogram of mixture. The term NG corresponds to the count of gases and, as explained before, NS is the number of species within the mixture. Within the framework of CEA, species are categorized by index: gases are assigned indices ranging from 1 to NG, while condensed species are designated indices between NG + 1 and NS. This understanding of the heat capacity, delineated through its various components, helps to better grasp the evolving nature of heat transfer and energy exchange within a system that undergoes chemical reactions. For more details, it is recommended that the reader refers to the technical notes of Gordon *et al.* [21].

Similarly to density, specific heat capacity is incorporated as a UDF in Ansys Fluent. Figure 5.3 illustrates the curves of c_p derived from CEA at a pressure of 1 bar.

5.1.3. Thermal Conductivity

In a manner analogous to heat capacity calculations, the determination of thermal conductivity also involves partitioning into frozen and reactive components according to the explanations by Gordon *et al.* [22]. This partitioning is denoted by the following equation:

$$\kappa = \kappa_f + \kappa_r \quad (5.7)$$

The frozen thermal conductivity, κ_f , is calculated using the formulation:

$$\kappa_f = \sum_{i=1}^{NM} \frac{x_i \kappa_i}{x_i + \sum_{j=1, j \neq i}^{NM} x_j \psi_{ij}} \quad (5.8)$$

Here, NM signifies the count of gaseous species, while x_i represents the mole fraction of species i within the mixture. The interaction coefficient ψ_{ij} , which captures species interactions, plays a central role in this calculation. It is governed by a formulation presented in the literature [22] and is essential for obtaining accurate thermal conductivity values.

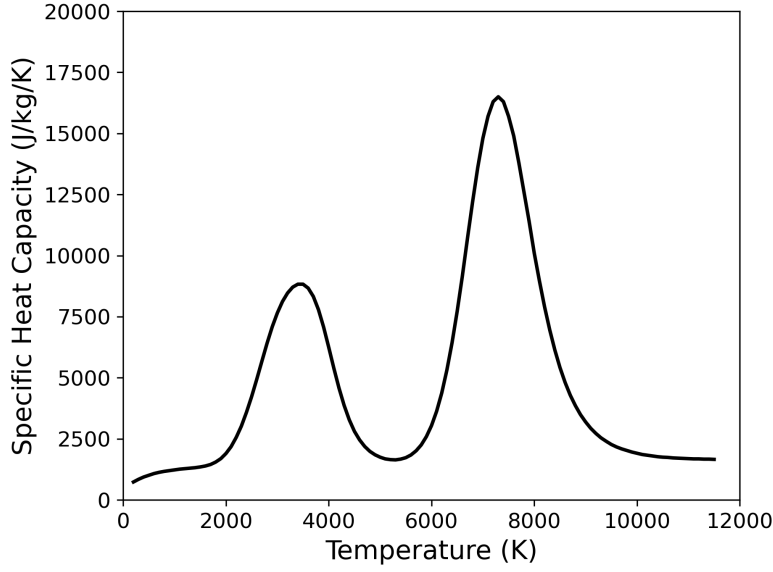


Figure 5.3.: Specific heat capacity at $p = 1000$ mbar

$$\psi_{ij} = \phi_{ij} \left[1 + \frac{2.41(M_i - M_j)(M_i - 0.142M_j)}{(M_i + M_j)^2} \right] \quad (5.9)$$

Within this equation, M_i represents the molecular mass of species i , and ϕ_{ij} is an additional interaction coefficient, as described by:

$$\phi_{ij} = \frac{1}{4} \left[1 + \left(\frac{\mu_i}{\mu_j} \right)^{1/2} \left(\frac{M_j}{M_i} \right)^{1/4} \right]^2 \left(\frac{2M_j}{M_i + M_j} \right)^{1/2} \quad (5.10)$$

Here, μ_i signifies the dynamic viscosity of species i .

The contribution of the reaction to the thermal conductivity was obtained by Butler and Brokaw [23] and implemented in CEA by McBride [21].

$$\kappa_r = R \sum_{i=1}^{\text{NR}} \frac{\Delta H_i^o}{RT} \kappa_{r,i} \quad (5.11)$$

NR denotes the number of chemical reactions of gaseous species, and ΔH_i^o is the enthalpy of reaction i at the temperature T . R is the gas constant. $\kappa_{r,i}$ are obtained by solving a set of linear equations.

$$\sum_{i=1}^{\text{NR}} g_{ij} \kappa_{r,j} = \frac{\Delta H_i^o}{RT} \quad (5.12)$$

The way of obtaining g_{ij} is explained by Gordon *et al.* [21]. Similarly to other properties, thermal conductivity can be implemented as a UDF in Ansys Fluent. Figure 5.4 shows the curves of κ obtained from CEA at a pressure of 1 bar.

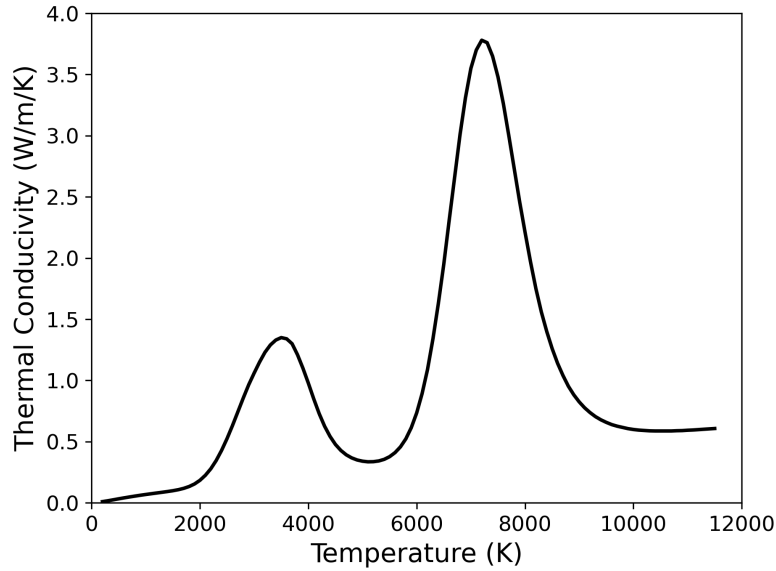


Figure 5.4.: Thermal conductivity at $p = 1000$ mbar

5.1.4. Dynamic Viscosity

The viscosity of the mixture is presented by Wilke *et al.* [24] and is given by:

$$\mu = \sum_{i=1}^{NM} \frac{x_i \mu_i}{x_i + \sum_{j=1, j \neq i}^{NM} x_j \phi_{ij}} \quad (5.13)$$

ϕ_{ij} is obtained from Equation 5.10. Similar to the other properties mentioned, viscosity is obtained by CEA as a function of temperature and pressure. Figure 5.5 shows the viscosity values as a function of temperature for the pressure of 1000 mbar. Viscosity is incorporated in Ansys Fluent by defining it as a UDF.

5.2. Fluid Properties Fitting for Fluent

The properties of the gas mixture are explored using CEA software. Figures 5.1 to 5.5 show the temperature-related changes of the properties of the gas mixture at a specific pressure of 1000 mbar. However, the main objective is to compile a comprehensive database across

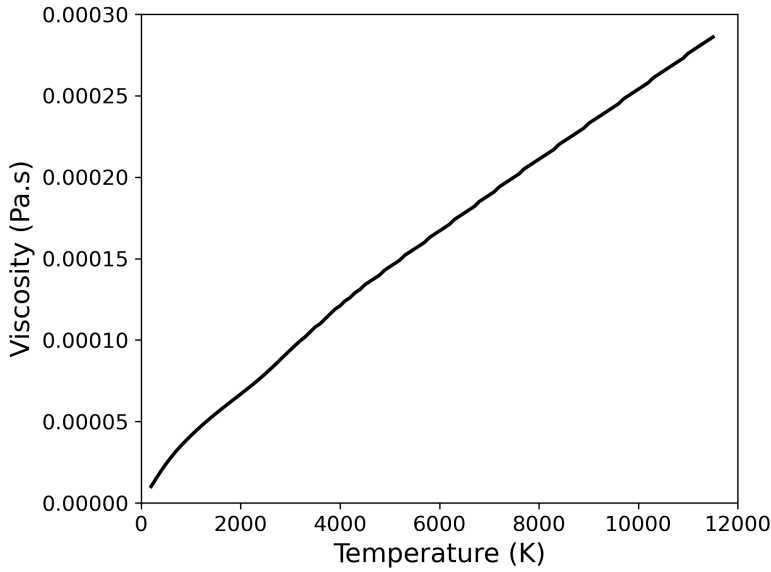
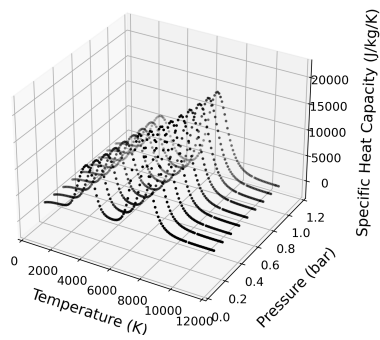


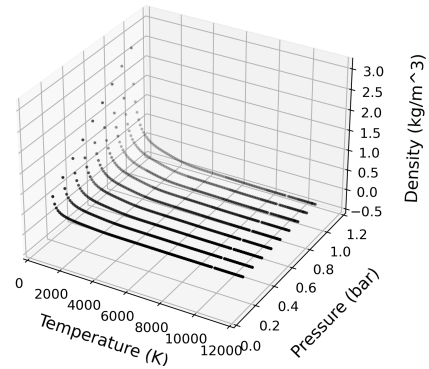
Figure 5.5.: Dynamic viscosity at $p = 1000$ mbar

pressures ranging from 200 mbar to 1000 mbar. The properties of the gas mixture for every 100 K within the temperature range of 200 K to 11 500 K are collected, and similarly for every 100 mbar within the specified pressure range. Figures 5.6a to 5.6f illustrate the patterns of each parameter in relation to both pressure and temperature. It is clear from the graphics that it is only possible to obtain a finite collection of three-dimensional data points for each gas property. However, in the context of Ansys Fluent, a continuous representation of each property is required as a function of temperature and pressure $f(T, p)$ to implement them as UDFs. Handling two-dimensional data based solely on temperature could include splitting the temperature range and approximating the data with higher-degree polynomials, e.g. by the use of cubic splines. However, fitting surfaces in three-dimensional space is difficult. The capability of neural networks is utilized to overcome this difficulty. A fully connected neural network is used to produce nonlinear output in the three-dimensional space [25]. The algorithm is developed in Python using the Keras library and, after training the model, converted to a C-based feedforward network to be compiling as a UDF in Fluent [26]. A sample of the feedforward network is available in the Appendix A

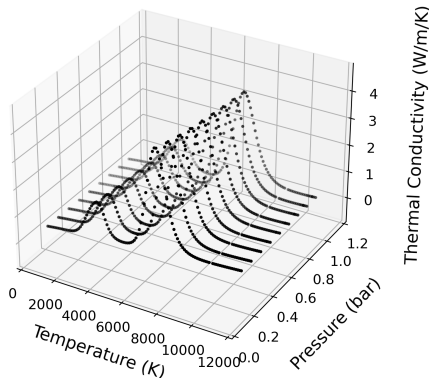
Each entry within the data set is characterized by an input and an output. The input consists of a two-dimensional vector, denoted $x_i = (T_i, p_i)$, where i represents the index of the point. The solution, labeled y_i , signifies the value of the specific gas property at the index i . To translate x_i into y_i , a six-layer neural network is employed. The network output is labeled \tilde{y}_i . The final goal is to find \tilde{y}_i so that it is as close to y_i . Therefore, the network requires modifiable parameters within each layer: weights (w) and biases (b). In each layer, the output from the preceding layer is multiplied by a weight matrix, followed



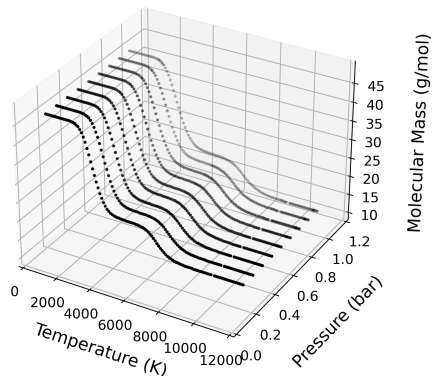
(a) Specific heat capacity



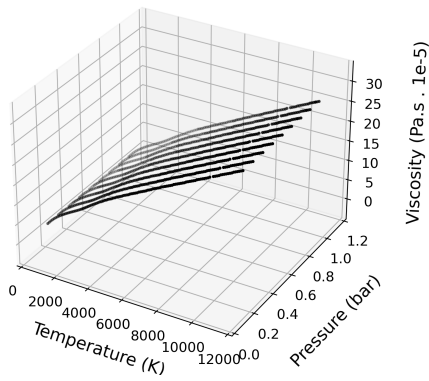
(b) Density



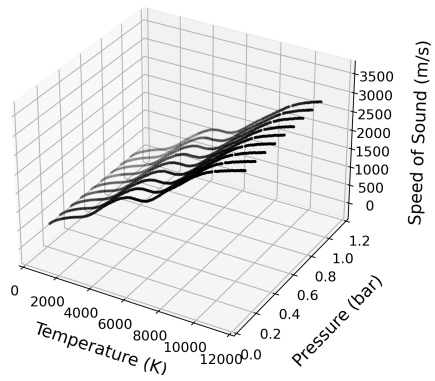
(c) Thermal Conductivity



(d) Molecular mass



(e) Viscosity



(f) Speed of sound

Figure 5.6.: Mixture properties for different temperature and pressures obtained from CEA.

by summation with a bias vector, enabling the network to fine-tune these connections and adapt the data representation.

$$s_j = w_j^T x_i + b_j \tag{5.14}$$

s_j is the output of this linear function where j denotes the number of the layer. In order to generate non-linearity, after implementing the linear function at each layer, exponential linear unit (ELU) activation functions are used.

$$a(s_j) = ELU(s_j) = \begin{cases} s_j & s_j \geq 0 \\ \alpha(e^{s_j} - 1) & s_j < 0 \end{cases} \tag{5.15}$$

Here, α is a constant that changes the angle of the function, and is equal to 1 by default in Keras. Figure 5.7 illustrates the forward feed process and the way input data change by passing through layers. The loss function of the norm $L2$ was used to assess the convergence between the calculated values \tilde{y}_i and the actual gas properties y_i . This function quantifies the difference between the anticipated and real values. Adam Optimizer was used to modify and optimize the network parameters [27].

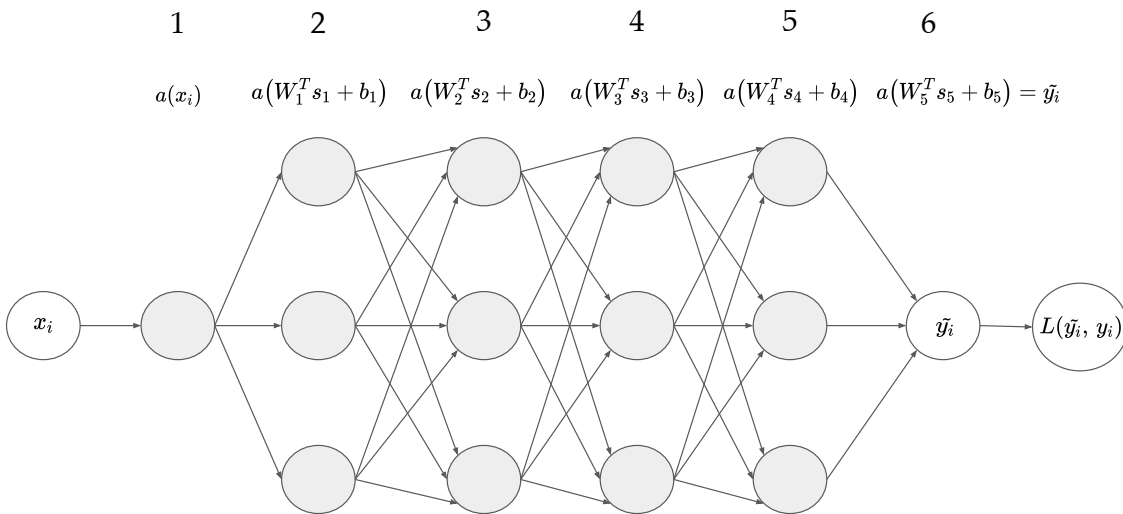


Figure 5.7.: Schematic of neurons and layers in the feed forward process.

5.3. Volumetric Heat Source

Obtaining a correct energy transfer of the microwaves to the reactor is one main objective of this work. As explained earlier in the beginning of this thesis (Chapter 2), during the

microwave discharge process, the gas moves through a tube made of quartz. In this setup, the quartz tube is positioned at the center of a resonator that is fed by microwaves coming from waveguides. After entering the resonator, the microwaves interact with the plasma contained within the quartz tube. During this interaction, the plasma absorbs the energy. To replicate the heat transfer process accurately, a new component is introduced into the energy equation 4.5. This new component is represented by a term for the power density (P_v) measured in watts per cubic meter. Essentially, this term serves as a representation of the heat source distributed throughout the three-dimensional space of the reactor.

$$\begin{aligned} P_v &= c \cdot f(r) \cdot g(z) , \\ 0 &\leq g(z) \leq 1 \end{aligned} \quad (5.16)$$

The power density is defined in terms of two coordinate directions: radial (r) and axial (z). The shape of the volumetric heat source is determined by two functions, $f(r)$ and $g(z)$, which dictate how the heat is distributed in the radial and axial directions, respectively. A normalization constant, denoted as c , is used to ensure that units are consistent and that the overall effect of the power density is appropriately scaled. The power absorbed by a plasma can be determined by integrating the power density throughout the plasma's volume.

$$\begin{aligned} P_{\text{MW}} &= 2\pi \int_0^{z_{pl}} \int_0^{r_{pl}} (P_v \cdot r) \, dr \, dz \\ &= 2\pi c \int_0^{z_{pl}} \int_0^{r_{pl}} [r \cdot f(r) \cdot g(z)] \, dr \, dz \end{aligned} \quad (5.17)$$

Here, P_{MW} is the microwave power that is absorbed by the plasma, z_{pl} and r_{pl} are the length and radius of the plasma respectively. Understanding the dimensions and shape of this heat source is crucial to an accurate simulation. The section continues to explain how the diameter and length of the plasma are determined, as well as how its radial and axial distribution within the reactor is characterized.

5.3.1. Heat Source Distribution in Radial Direction

The experimental research by D'Isa *et al.* shows that the diameter of the plasma scales linearly with the input of microwave power [9]. This means that as the power grows, so does the diameter of the plasma. D'Isa's research has resulted in the development of a fitting relation that provides a mathematical formula for calculating plasma diameter (in mm) depending on microwave power (in W).

$$d_{pl} = 0.002328 \cdot P_{\text{MW}} + 1.3851 \quad (5.18)$$

According to observations made by Wolf *et al.*, the distribution of the plasma in the radial direction (denoted here as $f(r)$) follows a Gaussian distribution [10]. As a result, the

following equation can be derived:

$$f(r) = e^{\frac{-r^2}{2\sigma^2}} \quad (5.19)$$

Here, standard deviation represented as σ . It is important to note that the highest power density is on the center line of the plasma, and this is denoted as follows:

$$P_v(r = 0, z) = c \cdot g(z)_{max} = c \quad (5.20)$$

The plasma diameter is specified as the width where the power density is only 15% of the maximum [9]. By implementing Equation 5.19 into Equation 5.16, the following equation can be derived.

$$0.15 \cdot c = c \cdot e^{\frac{-r_{pl}^2}{2\sigma^2}} \quad (5.21)$$

$r_{pl} = d_{pl}/2$ is the plasma radius, and by solving this equation, the standard deviation is obtained.

$$\sigma = \frac{d_{pl}}{2\sqrt{-2\ln(0.15)}} \quad (5.22)$$

Figure 5.8 illustrates the power density distribution in the radial direction for $g(z) = 1$.

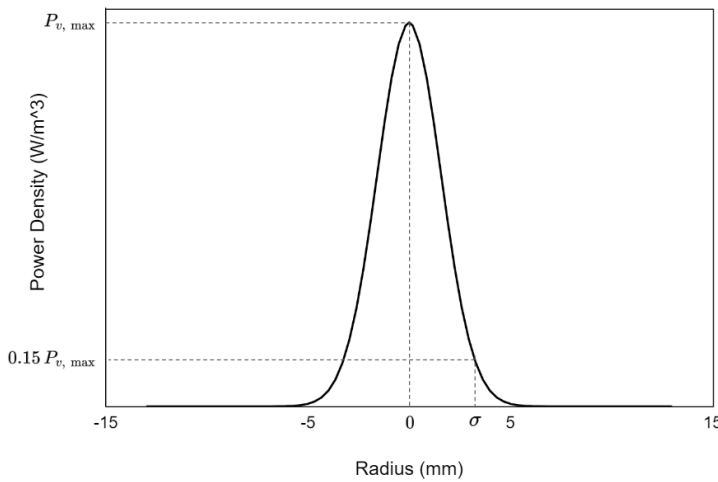


Figure 5.8.: Schematic of neurons and layers in the feed forward process.

5.3.2. Heat Source Distribution in Axial Direction

Using D'Isa's experimental results, it was discovered that the length of the plasma responds linearly to variations in power input [9]. Unlike the diameter, which does not appear to be affected by pressure changes, plasma length was observed to increase with

pressure changes [9]. This equation gives a method for estimating plasma length (in mm) based on microwave power input (in W) and pressure (in mbar).

$$z_{pl} = 0.01716 \cdot P_{MW} + 0.04432 \cdot p + 6.703 \quad (5.23)$$

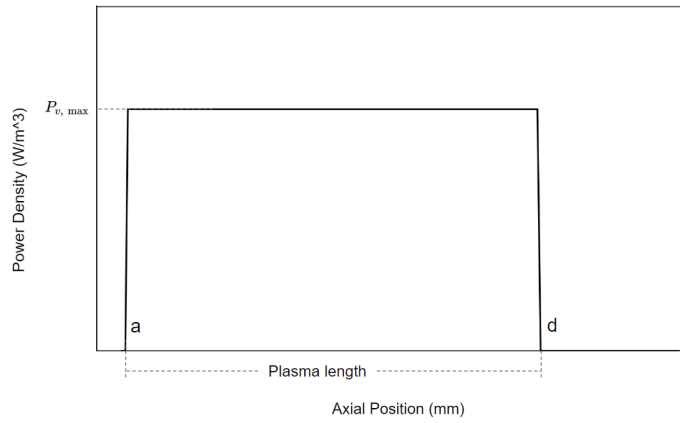
z_{pl} is the length of the plasma. The plasma distribution along the axial direction, denoted by $g(z)$, is not well understood by researchers. As a result, an approach including sensitivity analysis in various plasma shapes in the axial direction needs to be employed. This method helps to investigate and comprehend the effect of various plasma shapes in this direction on the temperature distribution. Therefore, three cases are expressed, which are shown in Figure 5.9. Case I considers the constant value of $g(z) = 1$ in the plasma region a to d shown in Figure 5.9a and zero for the other axial positions. In case II, which is shown in Figure 5.9b, $g(z)$ is defined as a piecewise expression. This function consists of two polynomial sections with a degree of three, and there is a constant function in between. In order to have a smooth transition between the sections, $dg/dz = 0$ at the points a , b , c , and d .

$$g(z) = \begin{cases} 0 & z < a \\ k_1 z^3 + k_2 z^2 + k_3 z + k_4 & a \leq z < b \\ 1 & b \leq z < c \\ k_5 z^3 + k_6 z^2 + k_7 z + k_8 & c \leq z < d \\ 0 & d \leq z \end{cases} \quad (5.24)$$

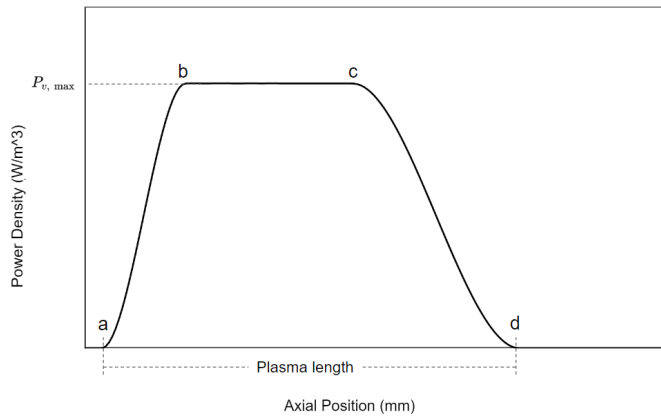
Here, k_1 to k_8 are coefficients that need to be find based a , b , c , and d values. a is the point at which the plasma begins. The assumption is that it is located 1 mm above the brass pin. The point d is where the plasma ends and the points b and c are defined by the user. This study considers $b = 0.2z_{pl}$ and $c = 0.6z_{pl}$ as an initial guess.

Case III is an ellipse with a maximum value of $g(z) = 1$ in the middle. For simplicity, $\hat{z} = z - a$ is defined so that the ellipse of Figure 5.9c starts from the origin with the transformed coordinate.

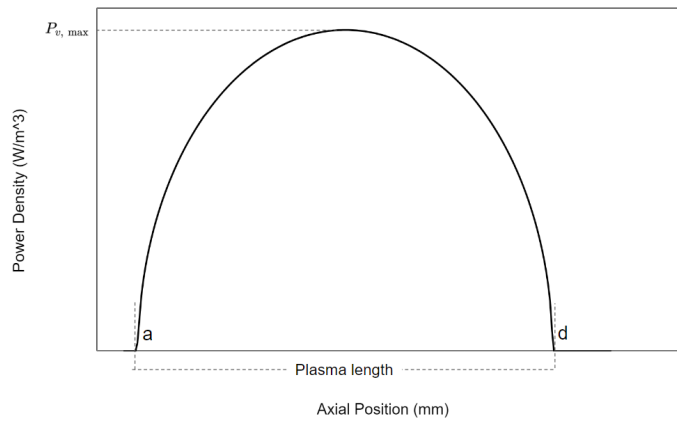
$$g(\hat{z}) = \sqrt{1 - \left(\frac{\hat{z} - \frac{z_{pl}}{2}}{\frac{z_{pl}}{2}} \right)^2} \quad (5.25)$$



(a) Case I



(b) Case II



(c) Case III

Figure 5.9.: Potential axial distributions of plasma.

6. Turbulence Model

Turbulence plays a significant role in shaping the way fluids move, although understanding its intricacies poses challenges. Before employing turbulence models in simulations, it is crucial to determine whether the reactor flow is characterized by turbulence or laminar behavior. Although flow dynamics vary between distinct regions, special attention is warranted for the specific areas of 1 and 2 illustrated in Figure 6.1, located near the plasma, the quartz tube, and the pin. This region is of particular importance due to its potential to exhibit complex flow interactions. Estimating the Reynolds number helps to understand the flow regime. Region 1 is where the gas is pure CO₂. Region 2 on the other hand, is where the gas temperature increases and dissociation occurs. As the properties of gas are different in these two regions, the turbulence is analyzed separately in these two regions.

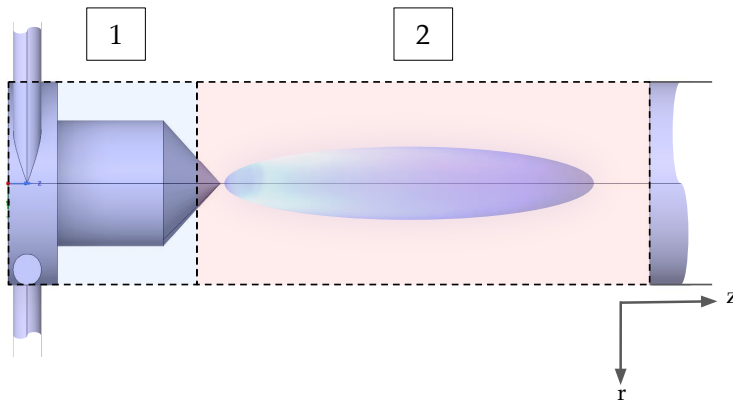


Figure 6.1.: Schematic of the reactor near the quartz tube.

The Reynolds number in a pipe or duct is expressed as:

$$\text{Re} = \frac{\rho \cdot U \cdot D}{\mu} \quad (6.1)$$

U is the mean flow velocity and D is the characteristic hydraulic diameter of the pipe or duct [28]. Hydraulic diameter is considered to be the diameter of the cross section of the quartz tube (26 mm). The formula for calculating the mean velocity is as follows:

$$U = \frac{1}{A} \int |\vec{u}| ds \quad (6.2)$$

Here, A is the cross section area and $|\vec{u}|$ denotes the velocity magnitude at different points of that cross section. To compute this parameter, the operating condition needs to be selected first.

This study aims to verify its findings using experimental data provided by Kiefer *et al.* [12]. Therefore, the flow follows the following settings: a standard flow rate CO₂ of 7 slm, operating at a pressure of 200 mbar and an inlet temperature of 300 K. By conducting initial simulations, a mean velocity of around 5 m/s in both regions of 1 and 2 can be approximated. Thus, the Reynolds number in region 1 (Re_c) can be estimated as follows:

$$Re_c = \frac{0.353[\text{kg}/\text{m}^3] \cdot 5[\text{m}/\text{s}] \cdot 0.026[\text{m}]}{1.5 \times 10^{-5}[\text{Ns}/\text{m}^2]} \approx 3060 \quad (6.3)$$

Within region 2 at the reactor's center, the temperature registers around 6000 K. Progressing toward the walls, this temperature diminishes, leading to rapid changes in density and viscosity. This gives rise to diverse flow patterns and consequently different Reynolds number values. However, as the temperature is elevated in region 2, the density is lower and the viscosity is higher. As a result, the Reynolds number is reduced in this area in contrast to region 1. For instance, the Reynolds number close to the plasma (Re_{pl}) can be estimated as follows:

$$Re_{pl} = \frac{0.0085[\text{kg}/\text{m}^3] \cdot 5[\text{m}/\text{s}] \cdot 0.026[\text{m}]}{1.67 \times 10^{-4}[\text{Ns}/\text{m}^2]} \approx 6.6 \quad (6.4)$$

The threshold value for the Reynolds number for the transition from laminar to turbulent flow in a pipe is typically around 2000. This means that if the Reynolds number is below 2000, the flow is more likely to be laminar, while if it is above this value, the flow is more likely to be turbulent [28]. It can be inferred that the flow in region 1 is likely turbulent, but determining the flow regime near the plasma region poses challenges. Despite our estimates indicating a low Reynolds number, making a definitive conclusion about the transition from turbulence to laminar flow in that region is not easy. Nevertheless, confirming the presence of turbulence in region 1 is sufficient for our decision to employ turbulent models in the simulations. The attributes of the upstream flow exert a significant influence on the behavior of the plasma. Increased upstream flow velocities result in lower plasma temperatures since the flow moves faster inside the plasma, consequently there is less time for energy transfer.

In general, there are three main approaches to include turbulence in simulations. Direct numerical simulation (DNS) simulates turbulent flows with the highest level of detail and accuracy within the constraints of current computational resources [19]. DNS solves the equations of 4.2 to 4.7 for a very fine mesh that is computationally intensive. The alternative approach is large-eddy simulation (LES), a turbulence modeling technique used to simulate turbulent flows with an emphasis on capturing larger-scale turbulent structures while modeling smaller-scale structures. Large-scale turbulent structures are resolved directly without modeling by solving the Navier-Stokes equations for these structures [29].

This model strikes a balance between extremely detailed but computationally costly DNS and more practical but less detailed Reynolds-averaged approaches (RANS). RANS models for the simulations are used. The primary concept in RANS simulations is the Reynolds decomposition, which divides the velocity, pressure, and other flow variables into two parts: Mean flow ($\bar{\phi}$), and turbulent fluctuations (ϕ') [30].

$$\phi = \bar{\phi} + \phi' \quad (6.5)$$

By breaking down the variables in Equations 4.2 to 4.7, averaging them over time (and omitting the bar on the mean flow parameter $\bar{\phi}$), the Reynolds-Averaged Navier-Stokes (RANS) equations can be expressed in Cartesian tensor form like this [31]:

$$\frac{\partial}{\partial x_i}(\rho u_i) = 0 \quad (6.6)$$

$$\frac{\partial}{\partial x_j}(\rho u_i u_j) = -\frac{\partial p}{\partial x_i} + \frac{\partial}{\partial x_j} \left[\mu \left(\frac{\partial u_i}{\partial x_j} + \frac{\partial u_j}{\partial x_i} - \frac{2}{3} \delta_{ij} \frac{\partial u_k}{\partial x_k} \right) \right] + \frac{\partial}{\partial x_j} \left(-\rho \overline{u'_i u'_j} \right) \quad (6.7)$$

$$\frac{\partial}{\partial x_i} [u_i(\rho E + p)] = \frac{\partial}{\partial x_j} \left(\kappa_{eff} \frac{\partial T}{\partial x_j} + u_i(\tau_{ij})_{eff} \right) + P_v \quad (6.8)$$

Equations 6.6 to 6.8 denote the conservation of continuity, momentum, and energy in RANS models respectively. δ_{ij} in Equation 6.7 is the Kronecker delta. In this equation, the term $\overline{u'_i u'_j}$ is the Reynolds stress, which has been discussed for many years. Next section explains how to compute it. E in Equation 6.8, is the total energy and κ_{eff} is the effective thermal conductivity. It consists of the laminar (κ) and turbulent (κ_t) parts.

$$\kappa_{eff} = \kappa + \kappa_t \quad (6.9)$$

κ is defined by user and is extracted using CEA as explained in Chapter 5. Fluent computes κ_t and automatically adds it to the user-defined thermal conductivity.

$$\kappa_t = \frac{c_p \cdot \mu_t}{Pr_t} \quad (6.10)$$

μ_t is the turbulent viscosity which is explained in the next section. Pr_t denotes the turbulent Prandtl number that is equal to 0.85 by default [18]. In Equation 6.8, $(\tau_{ij})_{eff}$ is the deviatoric stress tensor represented as:

$$(\tau_{ij})_{eff} = \mu_{eff} \left(\frac{\partial u_j}{\partial x_i} + \frac{\partial u_i}{\partial x_j} \right) - \frac{2}{3} \mu_{eff} \frac{\partial u_k}{\partial x_k} \delta_{ij} \quad (6.11)$$

Here, μ_{eff} is the effective viscosity and similar to effective thermal conductivity is represented by two parts of laminar and turbulent [18].

$$\mu_{eff} = \mu + \mu_t \quad (6.12)$$

The term $(\tau_{ij})_{eff}$ represents the viscous heating and is considered in the density-based solvers. It is not computed by default in the pressure-based solvers, as explained in Chapter 4, though one can activate it in Fluent [18].

6.1. Reynolds Stress

The Reynolds stresses term in Equation 6.7, denoted $\overline{u'_i u'_j}$, comprises six unknowns in a three-dimensional space. Since the total number of available equations is insufficient to fully characterize the system, methods that can effectively represent this term are required. A frequently used approach involves applying the Boussinesq hypothesis to establish a connection between Reynolds stresses and the mean velocity gradient [32].

$$-\overline{\rho u'_i u'_j} = \mu_t \left(\frac{\partial u_i}{\partial x_j} + \frac{\partial u_j}{\partial x_i} \right) - \frac{2}{3} \left(\rho k + \mu_t \frac{\partial u_k}{\partial x_k} \right) \delta_{ij} \quad (6.13)$$

In this context, the symbol k represents turbulent kinetic energy. The k - ϵ models and k - ω models employ this approximation, incorporating two additional transport equations for turbulent kinetic energy (k) and either dissipation rate (ϵ) or specific dissipation rate (ω) [33, 34]. As an alternative to Equation 6.13, the Reynolds Stress Model (RSM) takes a different approach. It solves transport equations individually for each of the Reynolds stresses, along with a transport equation to determine the scale (typically using ϵ or ω) [35].

Due to the swirling motion of the flow, the use of a suitable turbulence model that can capture this behavior is one of the goals of this study. To address this, four turbulence models of the Renormalization Group (RNG) k - ϵ , the Realizable k - ϵ , the Shear Stress Transport (SST) k - ω , and the Reynolds Stress Model (RSM) are used and compared to demonstrate their benefits and drawbacks in this study.

6.1.1. RNG k - ϵ Model

The RNG k - ϵ is a popular CFD turbulence model. It is an upgraded version of the standard k - ϵ model and is well known for its superior accuracy in predicting the behavior of turbulence near walls and in complex flows such as swirling flows. The letter "RNG" stands for "Renormalization Group," which is the mathematical technique utilized to improve the model's performance. Similarly to standard k - ϵ , this model solves two transport equations for turbulence variables: k and ϵ . These equations aid in the description of turbulence in a fluid flow. The model includes additional terms and coefficients developed from renormalization group theory [36]. For high Reynolds numbers, the turbulent viscosity is derived similarly to the Standard k - ϵ model as follows:

$$\mu_t = \rho \cdot C_\mu \cdot \frac{k^2}{\epsilon} \quad (6.14)$$

with $C_\mu = 0.0845$. However, this model performs better near walls for low Reynolds numbers compared to Standard k - ϵ model as it solves a differential equation to compute the turbulent viscosity for low Reynolds values. Based on the literature, this model performs better for swirling flow compared to the standard k - ϵ model [36].

6.1.2. SST k- ω Model

SST k- ω is an extension to the k- ω turbulence model that tries to provide reliable predictions for attached and separated turbulent flows. This model is good at simulating complex flow phenomena, such as boundary layer separation, unfavorable pressure gradients, and transitional flows. To describe how these turbulence variables change within the flow field, the SST k- ω model employs two transport equations, one for k and one for ω . These equations incorporate source terms to account for turbulence creation, diffusion, and dissipation. The "SST" in the model name refers to the inclusion of a particular term for turbulent shear stress transport. This factor contributes to the precision of the model near walls and in areas with unfavorable pressure gradients, where the standard k- ω model may not perform as well [37]. The turbulent viscosity in this model is derived by [18]:

$$\mu_t = \rho \cdot \frac{k}{\omega} \cdot \frac{1}{\max\left(\frac{1}{\alpha^*}, \frac{S \cdot F_2}{\alpha_1 \cdot \omega}\right)} \quad (6.15)$$

S is the strain rate and α^* is defined as a damp factor for turbulent viscosity which is equal to 1 for high Reynolds numbers and for low Reynolds numbers there is a specific formulation for it based on the literature [18]. $\alpha_1 = 0.31$, and $F_2 = \tanh \Phi_2^2$ where Φ_2 is given by:

$$\Phi_2 = \max\left[\frac{2 \cdot \sqrt{k}}{0.09 \cdot \omega \cdot y}, \frac{500 \cdot \mu}{\rho \cdot y^2 \cdot \omega}\right] \quad (6.16)$$

Here, y denotes the distance to the nearest next surface [18].

6.1.3. RSM Model

Even though both models of RNG k- ϵ , and SST k- ω perform better than their standard versions, they are still two-equation turbulence models, which means they assume that the turbulence is isotropic [38]. Isotropic turbulence refers to a type of turbulence in which the statistical properties of turbulence are the same in all directions at a given point in the flow of a fluid. In other words, in an isotropic turbulent flow, there is no preferred direction for turbulence fluctuations, and turbulence behaves similarly in all spatial directions [39]. Therefore, they have limitations in capturing anisotropic behavior, such as the strong rotational effects often present in swirling flows [38]. For more accurate simulations of swirling flows, researchers often turn to more advanced turbulence models such as RSM [35].

The RSM solves the transport equations for Reynolds stresses as well as an equation for the dissipation rate, to close the Reynolds-averaged Navier-Stokes equations. This means that seven more transport equations must be solved in 3D flows [35]. Reynolds stress models that rely on the ϵ equation, compute the turbulent viscosity μ_t in a manner analogous to how it is calculated in Equation 6.14 with $C_\mu = 0.9$ [18].

6.1.4. Realizable k- ϵ Model

The Realizable k- ϵ turbulence model differs from the standard k- ϵ model in two ways. For starters, it provides a different picture of turbulent viscosity. Second, the Realizable k- ϵ model incorporates a modified transport equation for the dissipation rate ϵ , which is derived from an exact equation [40]. This change improves the model prediction of turbulence dissipation, which is critical to understanding how turbulence expends energy when it interacts with flow. This model is particularly well suited for swirl flow because it accounts for anisotropic turbulence behavior more realistically than some other k-epsilon models [40]. Swirl flow is distinguished by fluid rotation, which can result in the production of complex turbulent structures.

6.2. Turbulence Models Comparison

This study performed simulations to compare the four turbulent models while analyzing the flow inside a reactor. In particular, no energy equation is solved in these simulations. Initially, at an operating pressure of 1000 mbar and a standard flow rate of 50 slm, all four simulations converged successfully. However, the interest in this thesis lay in simulating flows under lower pressure conditions down to 200 mbar. All four turbulent models are simulated for the standard flow rate of 7 slm. At this lower pressure, only the realizable k- ϵ and RSM models exhibited convergence. Therefore, only the results of these two turbulent models are shown in order to analyze the most accurate results.

Figure 6.2 illustrates the contours of the magnitude of the velocity within the reactor at the operating pressure of 200 mbar, specifically in the middle plane (XZ plane, where $Y = 0$). In particular, the RSM model showed slightly higher velocity magnitudes at the reactor entrance compared to the realizable k- ϵ model.

Furthermore, the turbulent viscosity was examined for both models. According to the literature, in the central core of the swirling flow, where the velocity gradients are lower and the flow is more stable, the turbulent viscosity tends to be lower than at surrounding locations [41]. Figure 6.3 shows the turbulent viscosity for both models. According to the figure, both models confirmed this trend, showing lower values in the middle. However, their specific trends are different.

A deeper analysis of turbulent viscosity from the center of the reactor ($r = 0$ mm) to its walls ($r = 13$ mm) at two axial points ($z = 50$ mm and $z = 160$ mm) is conducted. Figure 6.4 shows the trends of the turbulent viscosity ratio in the radial direction. The turbulent viscosity ratio μ^* is defined by the division of turbulent viscosity μ_t over laminar viscosity μ . In the RSM model, this value is highest near the walls and decreases significantly with movement away from the walls. In contrast, in the realizable k- ϵ model, it initially increased moving from the wall toward the center and then decreased as it approached the center. Additionally, the realizable k- ϵ model consistently exhibited higher turbulent viscosity values throughout the reactor compared to the RSM model. Based on the obser-

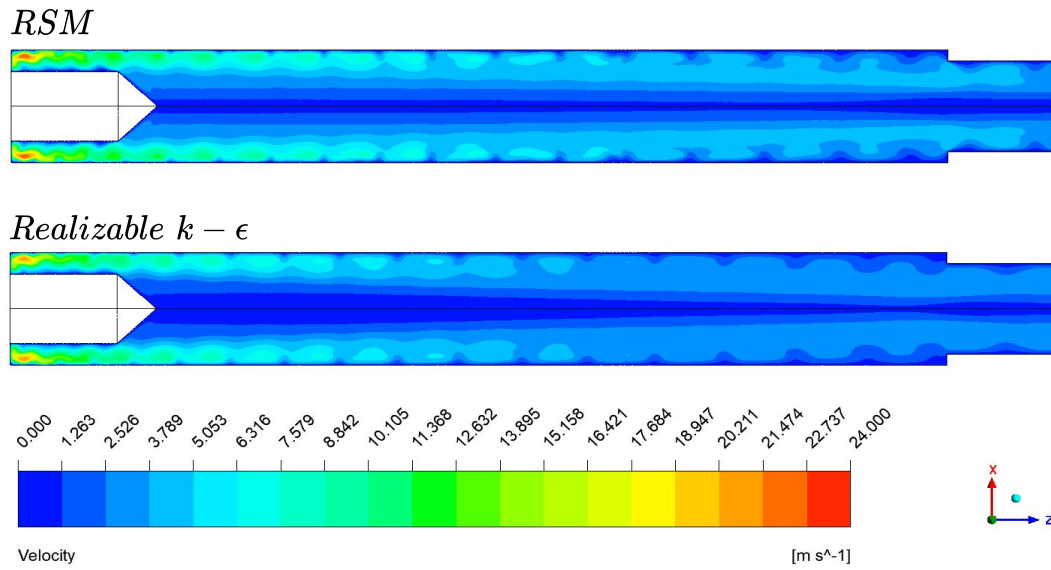


Figure 6.2.: Velocity contours at pressure 200 mbar and standard flow rate of 7 slm .

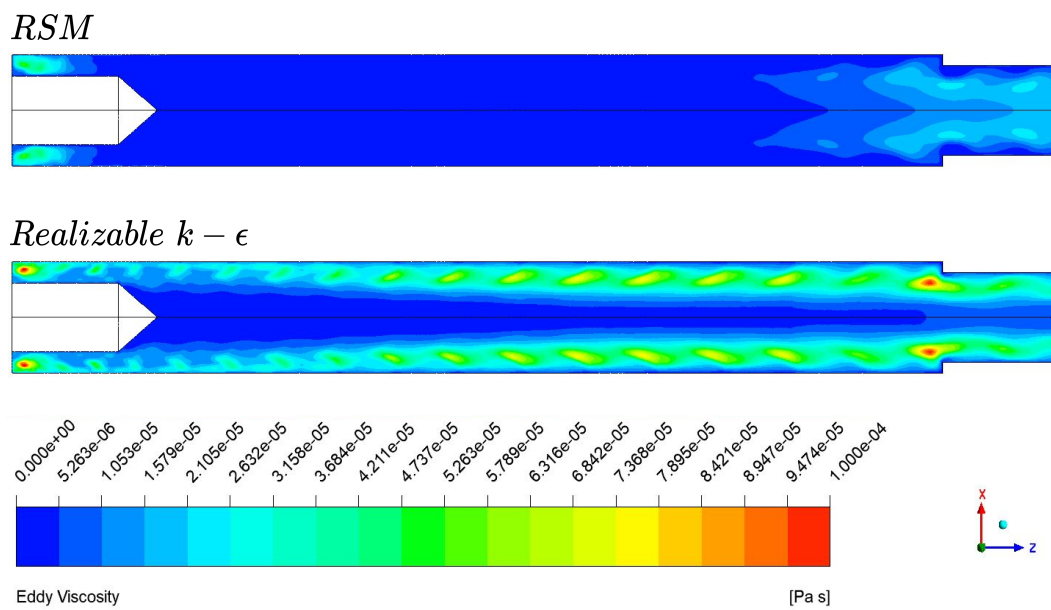


Figure 6.3.: Turbulent viscosity ratio at pressure 200 mbar and standard flow rate of 7 slm .

variations of Gupta *et al.*, the turbulent viscosity trend for a swirling flow in a pipe is closer to that of the realizable $k-\epsilon$ in the simulation [41]. As a result, the realizable $k-\epsilon$ model is used as the primary model for the simulations, and the RSM model is considered as an auxiliary model for comparison when necessary.

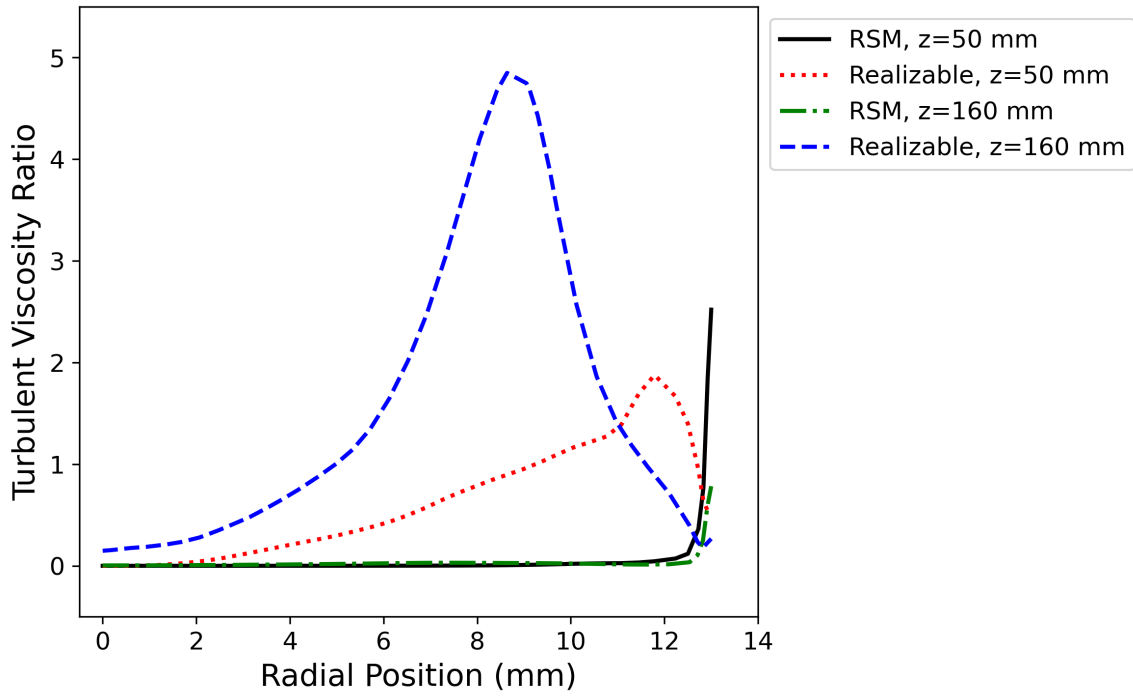


Figure 6.4.: Turbulent viscosity ratio at pressure 200 mbar and standard flow rate of 7 slm in the radial direction.

7. Boundary Conditions

This chapter provides a concise explanation of the process used to establish boundary conditions. Boundary conditions are essential parameters that define the scope and constraints of the research. In the following, inlet, outlet, walls, and periodic boundary conditions are explained.

7.1. Inlet

In the geometry of the reactor, there are four input tubes, each with a diameter of 4 mm. In the research by Kiefer *et al.*, the flow is expressed in terms of the standard gas flow rate (Γ_s) for their experiments [12]. However, for the sake of simplicity in simulations, this thesis decided to define the boundary conditions in terms of inlet velocity instead. To make this conversion from flow rate to velocity, a procedure is followed to ensure consistency in the modeling approach.

The real volumetric flow rate (Q), in SI unit, can be calculated from the standard gas flow rate as follows:

$$Q = \Gamma_s \cdot \frac{p_s}{p} \cdot \frac{T}{T_s} \cdot \frac{1}{1000 \cdot 60} \quad (7.1)$$

where $T_s = 273.15$ K and $P_s = 101\,325$ Pa. As there are four inlets, this value is divided by 4 to obtain the volumetric flow rate at each inlet. The inlet velocity is then computed as follows [14]:

$$u_{in} = \frac{Q}{4A_{in}} \quad (7.2)$$

where A_{in} is the cross section area at each inlet.

7.2. Outlet

In the simulations, a pressure outlet condition based on the research of the Kiefer experiment *et al.* is adopted at the boundary [12]. This condition ensures that the pressure at the outlet is maintained at specific values.

7.3. Wall

The no-slip boundary condition is applied for velocities on all walls. This condition assumes that the velocity of the fluid on the wall is zero, which is a common assumption for

viscous flow in fluid dynamics.

However, the heat transfer behavior can vary on different walls. Therefore, different approaches are used to model heat transfer on each wall boundary, taking into account the specific thermal properties and conditions associated with the material and geometry of each wall. This tailored approach ensures a more accurate representation of heat transfer in the simulation. To begin, we introduce the boundary conditions used on the wall.

Within the current study situation, boundary conditions on surfaces can be established in two ways. First, an exact temperature can be set for a wall. In this case, Fluent automatically computes the heat transfer rate to keep the temperature constant on the wall. This option is only possible when a rough estimate of the wall temperature is available. Alternatively, the heat transfer rate can be set on the wall. In this case, the determination is based on the amount of heat energy communicated between the surface and its surroundings over a given time period. In this process, the choice includes conduction, convection, or a mixture of these techniques. Conduction and convection heat transfers are implemented using the composition rule. This rule allows the total thermal resistance (R_{total}) of a wall to be calculated by adding the individual thermal resistances of each layer on the heat transfer path. Figure 7.1 gives a brief description of the change in temperature and heat transfer on a wall. In the following, a scenario is described in which Fluent takes into account both convection and conduction heat transfers. When this explanation is understood, it becomes straightforward to deduce situations that involve only convection or only conduction heat transfers.

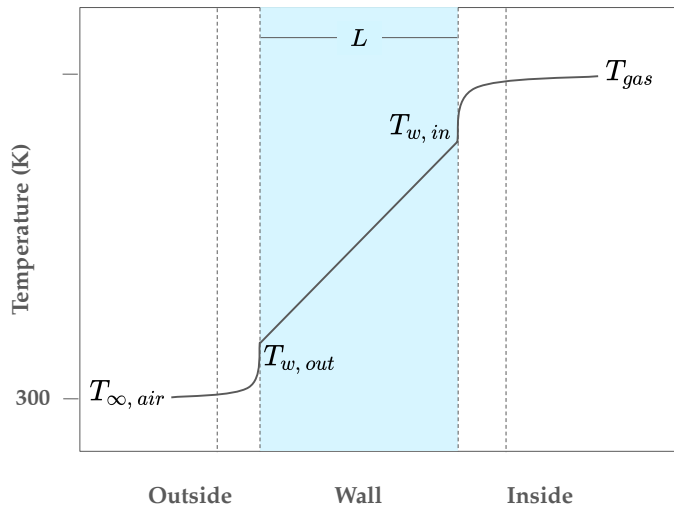


Figure 7.1.: Temperature change in the vicinity of the wall.

Heat transfer \dot{q} near the wall is defined by:

$$\dot{q} = \frac{A(T_{w,in} - T_{\infty,air})}{R_{total}} \quad (7.3)$$

Here A is the heat transfer area, $T_{\infty,air}$ denotes the ambient air temperature and is equal to 300 K, and $T_{w,in}$ is the temperature of the wall from inside, which is computed by Fluent [18]. R_{total} is defined as follows:

$$R_{total} = \frac{1}{h_{out}} + \frac{L}{\kappa} \quad (7.4)$$

h_{out} denotes the convection heat transfer coefficient of the air, κ is thermal conductivity of the wall material, and L is its thickness. To close the system, h_{out} need to be found. The heat transfer coefficient for air moving around a circular cylinder is as follows [16].

$$h_{out} = \frac{Nu \cdot \kappa_{air}}{D} \quad (7.5)$$

D is the outer diameter of the cylinder, κ_{air} represent the thermal conductivity of air, and Nu is the Nusselt number. Nusselt number can be derived on the basis of the thermodynamic sheets of the pipes. However, in this study, the following equation is used to obtain it [16].

$$Nu = 0.027Re^{0.805} \cdot Pr^{1/3} \quad (7.6)$$

Here, Pr is Prandtl number and is equal to 0.7 for air. Re is the Reynolds number and is computed by $(\rho_{air} \cdot U_{\infty,air} \cdot D)/\mu_{air}$. The density and viscosity of the air are known at the given temperature. Therefore, knowing the ambient velocity around the circular cylinder, the Reynolds number can be computed. As a result, on the basis of the descriptions provided above, there is a flexibility in choosing either temperature or heat transfer rate settings for the wall boundaries. In the following, the idea to select these boundary conditions is explained for each specific wall.

Figure 7.2 visually represents various wall boundaries utilized in these simulations. Wall 1 corresponds to the input tubes and the lower section of the reactor, where it is impossible to directly calculate the heat transfer. However, a temperature of 300 kelvin is assumed for these boundaries. Wall 2 refers to the ignition pin located near the plasma. Here, only conduction is considered as the mode of heat transfer for this wall. Wall 3 represents the quartz tube, and for its boundary, heat transfer is configured as a combination of convection and conduction, guided by Equation 7.5, to calculate h_{out} as input for Fluent. To determine the velocity of ambient air around this wall, this study relied on experimental data conducted by Kiefer *et al.* [12]. In their experiments, an air blower was used to externally cool the quartz tube, with a measured flow rate of 240 slm. Using the geometry depicted in Figure 7.3, we were able to calculate the air velocity in proximity to the outer surface of the quartz tube. The process of calculating the velocity from the standard flow rate is similar to the process of determining the inlet velocity in Section 7.1. Wall 4, in contrast, does not experience flow around it; therefore, conduction heat transfer for this wall is used exclusively. Wall 5 is enveloped by a larger tube containing cooling water. If there was information on the cooling water's velocity, it would be possible to estimate the heat transfer in a similar way to that applied for wall 3. However, due to limited information, it is assumed that the cooling process is efficient so that it maintains the wall temperature consistently at 300 K.

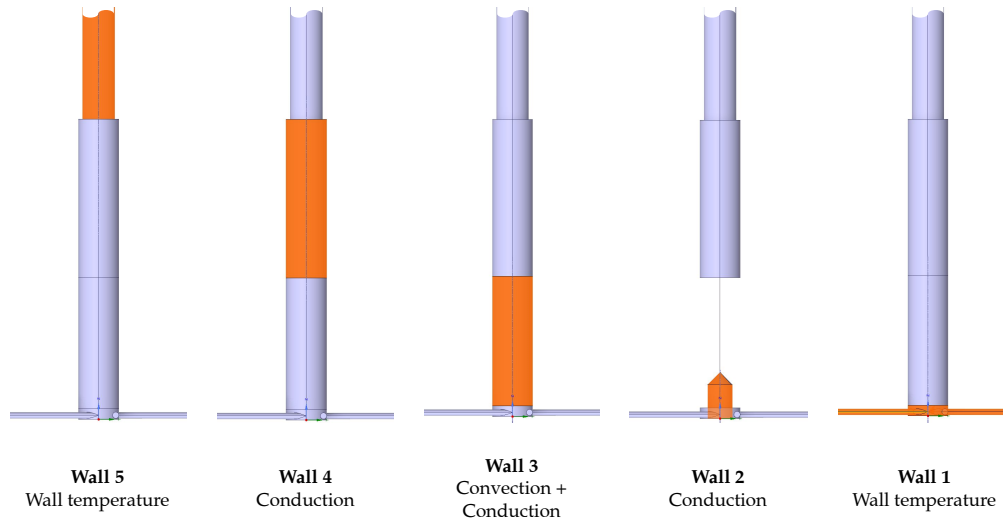


Figure 7.2.: Different types of specified wall boundaries for the simulation.

7.4. Periodic Boundary

When a system exhibits a repeating pattern in the flow distribution, periodic boundary conditions are used in fluid dynamics. If the pattern appears more than twice, it violates the mirror-image symmetry conditions, therefore, it can only be considered as a periodic boundary. A swirling flow inside a tube is an example of this, in which a given area repeats four times in angular coordinates. In such circumstances, the cyclic symmetric areas must preserve constant flow variables and distribution while also ensuring that this symmetry is maintained throughout all slices along the Z coordinate of the system.

When periodic boundary conditions are applied in Fluent, the software treats the flow at a periodic boundary as if the opposite periodic plane is a direct neighbor of the cells next to the first periodic boundary. In other words, it simulates the flow as if it is continuously moving from one side of the periodic boundary to the other. This method simplifies the simulation of periodic systems, allowing for effective modeling of repeated geometries or flow patterns [18]. Figure 7.4 shows the periodic boundaries in the model.

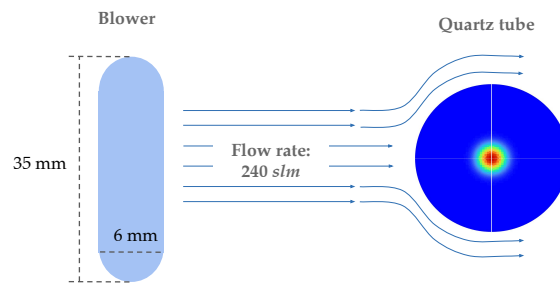


Figure 7.3.: The cooling process of quartz tube. The cross section of tip of the blower on the left.

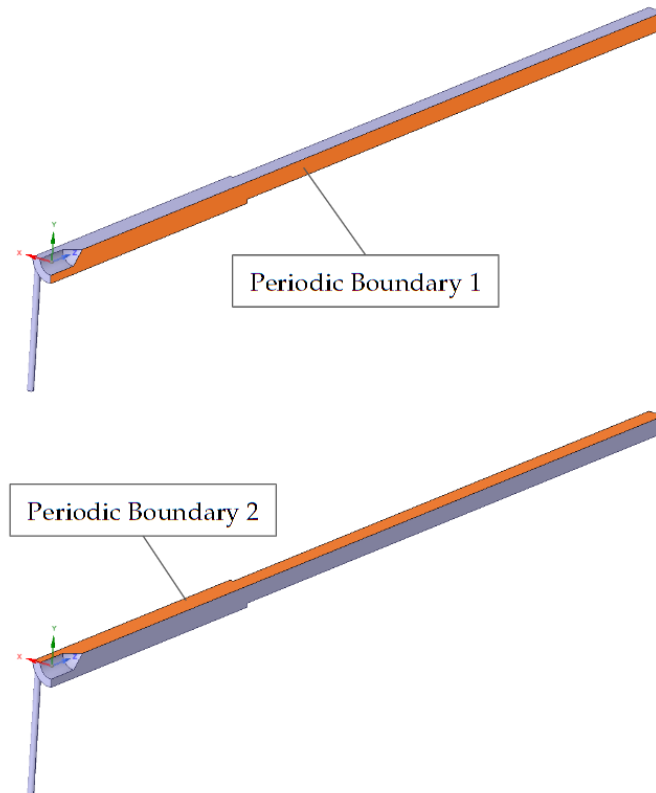


Figure 7.4.: Periodic boundaries of the quarter body

8. Results and Conclusion

In this chapter, the most significant findings of this thesis are presented. The results obtained under two different operating pressure conditions, 1000 mbar and 200 mbar, are shown, and the disparities between these results are highlighted. Subsequently, an analysis will be conducted to examine the potential parameters that could contribute to these variations. This analysis aims to provide information on the factors influencing the observed results at different pressure levels.

It is important to note that there are no experimental data available for comparison under the 1000 mbar pressure condition. Consequently, validation of these simulation results under this specific pressure condition is not feasible. However, as mentioned in previous sections, experimental data collected by Kiefer *et al.* exist for the temperature profile at an operating pressure of 200 mbar [12]. Therefore, Section 8.3 will dive into the results obtained under this condition and establish a comparison with the available experimental data.

8.1. Mesh Independence Study

In the grid study, six different grid sizes outlined in 3 were evaluated. These simulations were conducted at a standard flow rate of 7 slm and a pressure of 200 mbar. The average temperature value on the outlet boundary is considered for this examination. The reason is that it is influenced by the upstream flow conditions and all the cells within the simulation domain. Figure 8.1 illustrates this value.

Interestingly, the study found that there are limitations to the grid size on both ends of the spectrum. When the grids are too large, they struggle to accurately capture high-temperature gradients near the plasma, resulting in oscillatory behavior in that region. On the contrary, when the grid is too small, the swirling flow near the reactor walls becomes chaotic, leading to oscillations throughout the domain. In the middle range between these two extremes, a relative independence from grid size was observed. In particular, grid IDs 4 and 5 showed nearly identical temperature values. Consequently, grid ID 4 was chosen as the primary grid size for the simulations because it strikes a balance between accuracy and computational efficiency.

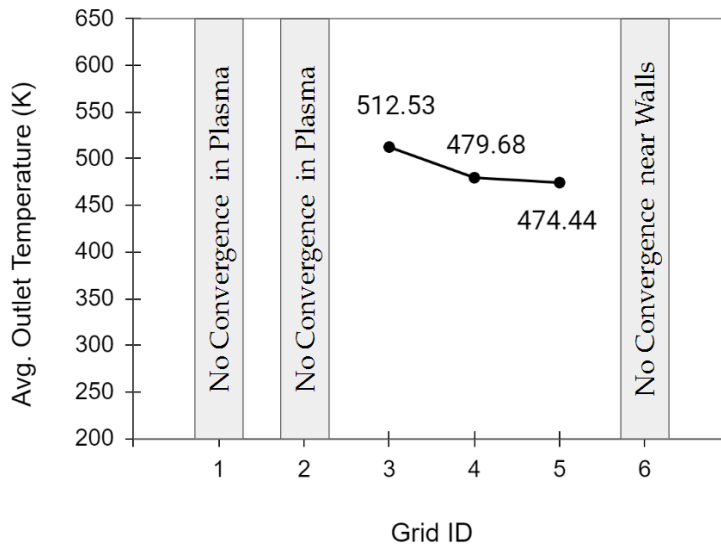


Figure 8.1.: Average temperature on the outlet surface.

8.2. Results at 1000 mbar

In this section, the simulation results are presented for the system operating at a pressure of 1000 mbar. The simulation assumes a standard flow rate of 50 slm and a power input of 2000 W. The diameter and length of the plasma are calculated from Equations 5.18 and 5.23. Figure 8.2 provides a visual representation of the contour of the temperature in the vicinity of the plasma.

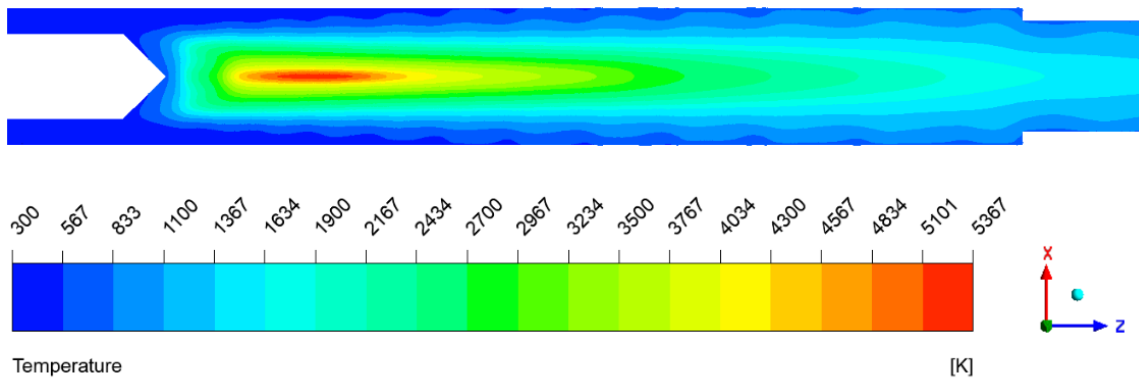


Figure 8.2.: Temperature contours at pressure 1000 mbar and standard flow rate of 50 slm .

Figure 8.3a shows temperature profiles along an axial line that passes through the center of the plasma, while Figure 8.3b illustrates temperature changes in the radial direction at the axial position where it crosses the middle of the plasma. The temperature profiles depicted in these figures exhibit a gradual transition along the axial and radial directions. In particular, the observed maximum temperature remains below 6000 K, consistent with the expected range.

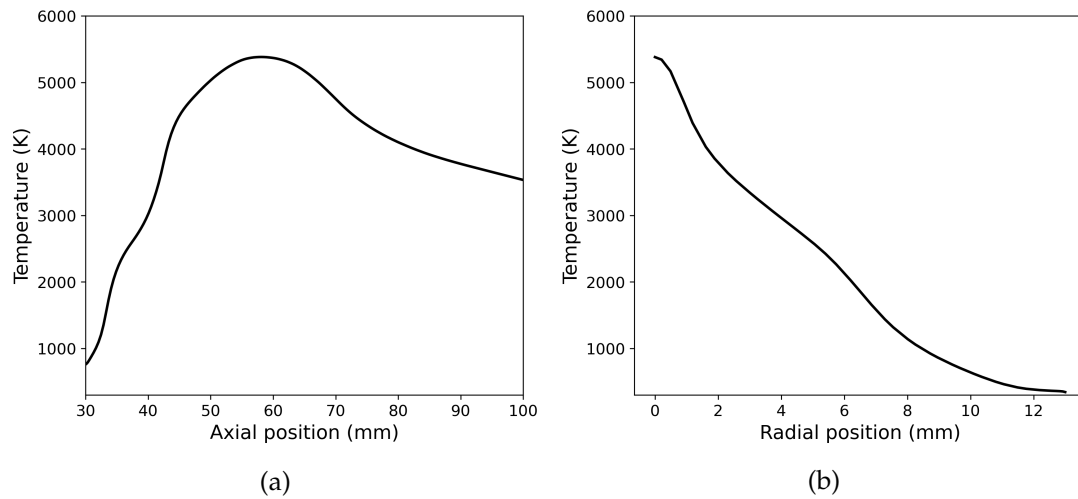


Figure 8.3.: Temperature profiles in the axial (left) and radial (right) directions.

8.3. Temperature Profile at 200 mbar

In this section, the simulation results are presented for the pressure of 200 mbar. The simulation assumes a standard flow rate of 7 slm and a power input of 1650 W. Figure 8.4 provides a visual representation of the contour of the temperature in the vicinity of the plasma. The size of the hot gas is much larger than that of 1000 mbar shown in 8.2. The temperature profile along the axial direction is compared with the experimental data of Kiefer *et al.* [12]. Figure 8.5 shows the temperature profiles along the axial line that passes through the center of the plasma. In the provided figure, there are notable differences between the simulated and experimental temperature data. First, the simulated temperatures consistently register values higher than those observed in actual experiments. Secondly, there are noticeable temperature gradients at the beginning and end points of the plasma in the simulated results. This abrupt temperature change is also reflected in the radial temperature profile shown in Figure 8.6. These disparities between the simulation and experiment results indicate areas where further investigation is necessary.

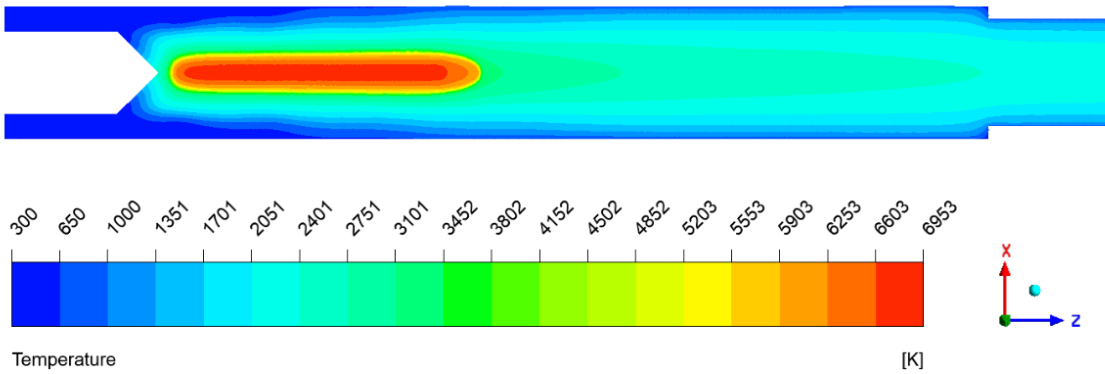


Figure 8.4.: Temperature contours at pressure 200 mbar and standard flow rate of 7 slm .

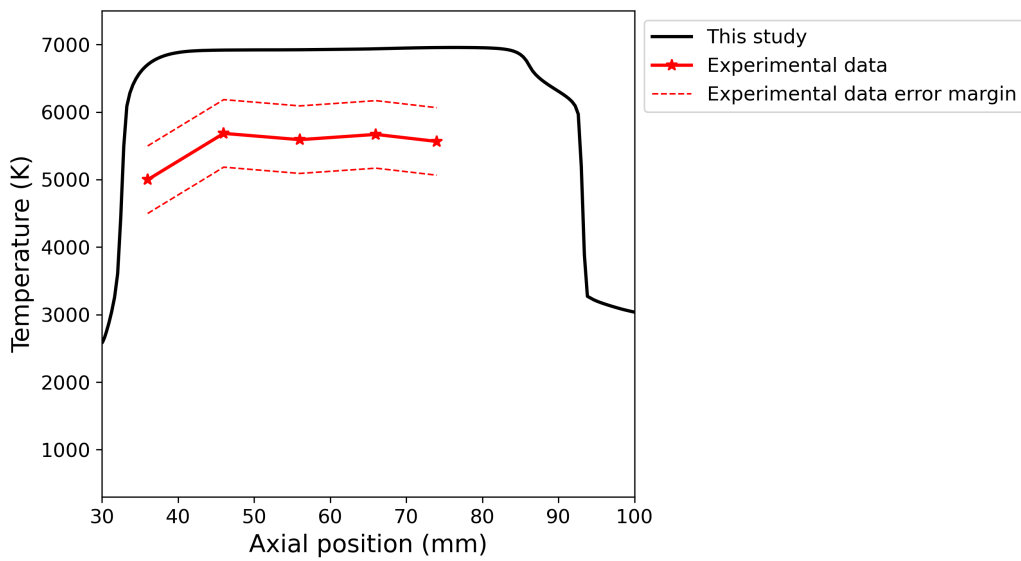


Figure 8.5.: Temperature profiles in the axial direction. The red lines represent the experimental data by Kiefer *et al.* [12].

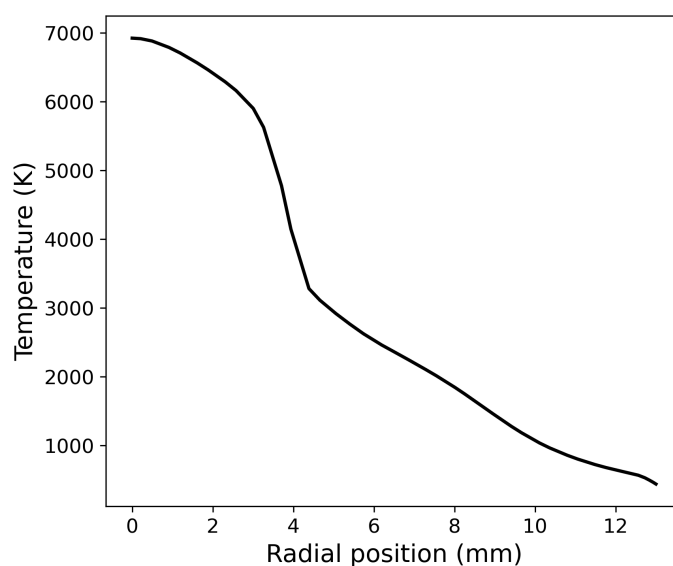


Figure 8.6.: Temperature profiles in the radial direction at the middle of the plasma

8.4. Sensitivity Analysis

In the presented data, two sets of results have been displayed, one for the 1000 mbar pressure condition and the other for the 200 mbar pressure condition. While the temperature profiles for the 1000 mbar condition generally remained within an acceptable range, staying below 6000 K, the results for the 200 mbar condition did not align well with the experimental data in terms of temperature magnitude. To address this discrepancy, this section aims to investigate the factors that can influence the temperature profiles. Specifically, it will analyze the impact of two key parameters: the choice of turbulence model and the heat source.

8.4.1. Effect of Turbulence Model

In Chapter 6 of the study, four turbulent models were discussed to simulate swirling flows. After careful evaluation, the realizable k - ϵ turbulence model was selected as the most suitable option for the simulations. However, it is important to note that in these simulations the energy equation was not solved and the interaction between the plasma and turbulence was not taken into consideration. To address this, the RSM model is included in the simulation for comparison. The results show that the turbulent model has little effect on the maximum temperature, but it can lower the temperature at the start of the plasma or change the volume of the hot gas.

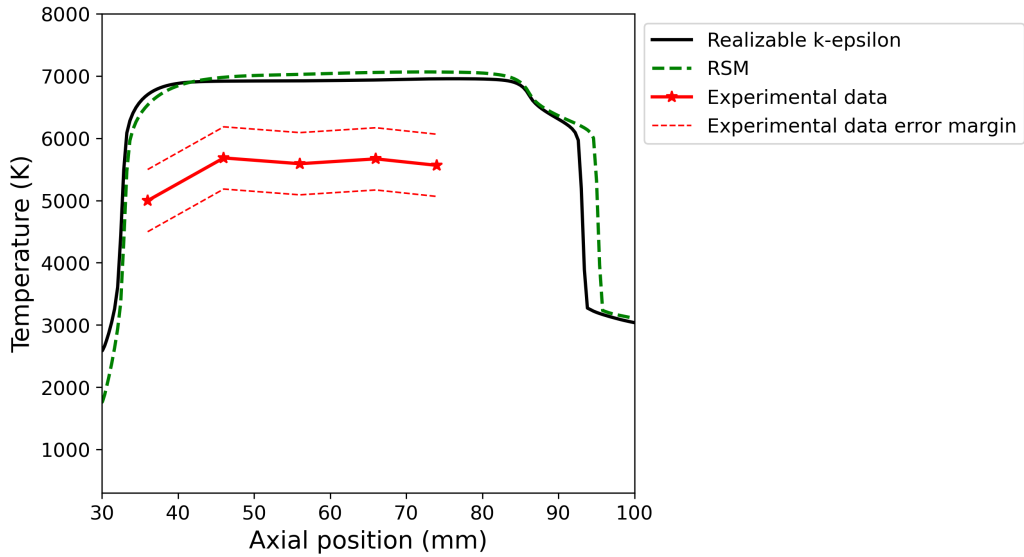


Figure 8.7.: Temperature profiles in the axial direction for RSM and Realizable k- ϵ models.

8.4.2. Effect of Heat Source

In Figures 8.5 and 8.6, a high-temperature gradient is evident at the outer boundary of the plasma. This observation raises the possibility that the heat source profile may be responsible for these pronounced gradients. Chapter 5 of the study describes the way to find the radial distribution of the heat source. However, an unknown in the study is the axial distribution of the heat source. To investigate this, three different axial heat source profiles are considered, as detailed in 5. The first assumption, called "case I," assumes a constant heat source profile. All of the results presented thus far are based on this initial assumption. Figure 8.8 compares the results of all three cases.

The observed temperature changes in response to different heat source profiles reveal interesting patterns. Specifically, when the heat source profile contracts in the middle, there is a notable temperature increase of 500 to 700 K within that region. On the contrary, at the beginning of the plasma, there is a temperature decrease. However, it is noteworthy that despite these variations in heat source profiles, all three cases exhibit the same temperature gradient at the end of the plasma.

This consistency in temperature gradient at the plasma's end strongly suggests that the observed variations are likely a numerical issue rather than a reflection of the underlying physics governing plasma and flow behavior. This finding underscores the importance of scrutinizing the numerical methods and parameters used in the simulation to ensure the accuracy of the results.

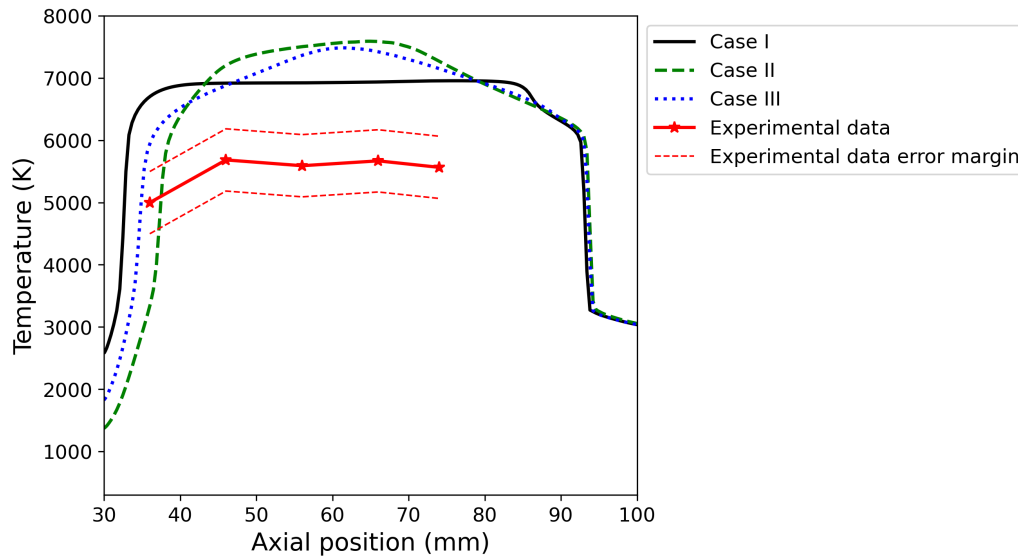


Figure 8.8.: Temperature profiles in the axial direction for different heat source cases of I, II, and III.

8.4.3. Velocity Profile Analysis

The sensitivity analysis conducted on different heat source shapes revealed a potential numerical stability issue under the operating condition of 200 mbar. This is investigated by comparing the velocity magnitude profiles along the axial direction for two cases: 200 mbar and 1000 mbar, with standard flow rates of 7 slm and 50 slm, respectively. After converting these flow rates to inlet velocities, it was found that the inlet velocity for the 200 mbar case was 12.91 m/s, while for the 1000 mbar case, it was 16.58 m/s. Figure 8.9 illustrates the results of this comparison, clearly showing a significant velocity jump at the end of the plasma for the 200 mbar condition. This abrupt change in velocity is attributed to numerical errors, highlighting the need for further investigation and potentially adjustments in the simulation setup to ensure numerical stability under this specific operating condition.

8.5. Conclusion

This thesis presented the development of a CFD model to simulate flow and heat transfer in a lab-scale microwave plasma torch for CO_2 dissociation. The model aimed to provide information on the temperature distribution within the plasma reactor under different operating conditions.

The geometry and mesh were constructed to represent a quarter of the actual experimental setup, taking advantage of symmetry to improve computational efficiency. The pressure-based coupled algorithm was selected as the solver due to the low Mach number

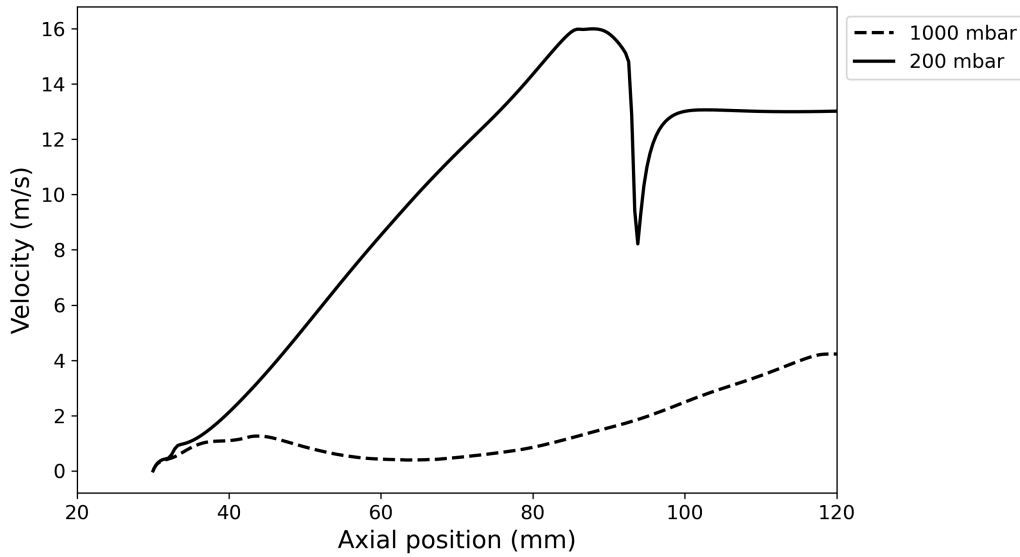


Figure 8.9.: Velocity profiles in the axial direction locating at the center of the plasma.

flow. The realizable k - ϵ and RMS turbulence models were chosen after evaluating their performance for swirling flows against other RANS models.

The model incorporated the dynamic properties of the gas mixture, including density, viscosity, thermal conductivity, and heat capacity as functions of temperature and pressure. This approach aimed to account for the effects of CO_2 dissociation without solving separate species transport equations and reaction equations. An additional volumetric heat source term was implemented to represent microwave energy absorption by the plasma.

The simulation results at 1000 mbar showed reasonable temperature profiles below 6000 K, aligning with expectations. However, at 200 mbar, the temperatures were predicted to be higher than in the experimental data, and sharp gradients existed at the plasma boundaries. Further sensitivity analysis indicated that neither the turbulence model nor the axial heat source distribution could explain these discrepancies.

Overall, the model provides a good foundation for simulating the microwave plasma torch. The overprediction of temperatures at 200 mbar warrants further investigation into possible numerical issues near high temperature gradients. As a suggestion for future research, it may be beneficial to create a finer local grid in the plasma region, as this has the potential to mitigate numerical errors. However, it is crucial to exercise caution during this process, considering the explanation provided in Section 8.1, which highlights the risk of flow instability near walls when using fine meshes.

Furthermore, since neither of the turbulent models used in the study was able to adequately explain the discrepancies in the solution, this raises the possibility that these models may not be effectively capturing the true flow behavior, which could be contributing to

numerical errors within the domain. As an alternative approach, optimization of these turbulent models is suggested. Although this study utilized the default Fluent values for all turbulent coefficients, further investigation of the actual physics of the tube and swirling flow is proposed to obtain more accurate coefficient values. For example, a potential task could involve refining the value of the turbulent Prandtl number, crucial for calculating turbulent thermal conductivity according to Equation 6.10, to better align with the real physical characteristics of the system.

Appendix

A. UDF Sample Code

The provided source code exemplifies a C-based feedforward network, illustrating the structure of a UDF file. In this case, the `DEFINE_PROPERTY` function from Fluent is used to calculate the thermal conductivity values. The code presented is hardcoded for clarity, with the aim of facilitating the reader's comprehension of the feedforward network. Other parameters such as density, specific heat capacity, sound speed, and viscosity are also determined using a similar procedure within the UDF. As can be seen in the algorithm, the parameters (w, b) which are derived by training the model in Python are implemented here as input.

A. UDF Sample Code

```
1 #include "udf.h"
2 #define Pressure 0.2 // 0.2 : P = 200 mbar
3
4 DEFINE_PROPERTY(thermalconductivity, c, t)
5 {
6     // Initialization
7     const int numLayers = 6;
8     const int maxNumNeurons = 3;
9     int row_w[numLayers], column_w[numLayers];
10    int row_l[numLayers], column_l[numLayers];
11    real w[numLayers][maxNumNeurons][maxNumNeurons];
12    real b[numLayers][maxNumNeurons];
13    real output[numLayers][maxNumNeurons][maxNumNeurons];
14    int layer, i, j, k;
15    real temperature = C_T(c, t);
16    real temp_mean = 5863.157895;
17    real temp_std = 3311.096991;
18    real pressure_mean = 0.6;
19    real pressure_max = 1.0;
20    real pressure_std = 0.258325;
21    real k_mean = 0.962224;
22    real x, y, z;
23    for (layer = 0; layer < numLayers; layer++)
24    {
25        for (i = 0; i < maxNumNeurons; i++)
26        {
27            for (j = 0; j < maxNumNeurons; j++)
28            {
29                output[layer][i][j] = 0.0;
30            }
31        }
32    }
33    // The model is trained for the normalized parameters, Therefore
34    // we need to normalize the input before putting the in,
35    // the feedforward network.
36    x = (temperature - temp_mean) / temp_std;
37    y = (Pressure - pressure_max) / pressure_std;
```

Source Code A.1.: Thermal Conductivity Computations Part 1/4

```

1 output[0][0][0] = x;
2 output[0][1][0] = y;
3 row_w[0] = 1;
4 column_w[0] = 1;
5 row_l[0] = 2;
6 column_l[0] = 1;
7 // Feedforward model
8 for (int layer = 1; layer < numLayers; layer++)
9 {
10     // Hard-coded weights and biases obtained by training
11     if (layer == 1)
12     {
13         w[layer][0][0] = -2.1398656;
14         w[layer][1][0] = 2.012015;
15         w[layer][2][0] = 3.608953;
16
17         w[layer][0][1] = 0.01207444;
18         w[layer][1][1] = -0.8753886;
19         w[layer][2][1] = -0.06030385;
20
21         b[layer][0] = -1.6653923;
22         b[layer][1] = -3.5867066;
23         b[layer][2] = -0.07474601;
24
25         row_w[layer] = 3;
26         column_w[layer] = 2;
27         row_l[layer] = 3;
28         column_l[layer] = 1;
29     }
30     else if (layer == 2)
31     {
32         w[layer][0][0] = 0.36729914;
33         w[layer][1][0] = 1.6734133;
34         w[layer][2][0] = 0.04253395;
35         w[layer][0][1] = 0.7093005;
36         w[layer][1][1] = -2.4906652;
37         w[layer][2][1] = 0.99602884;
38         w[layer][0][2] = 0.86852425;
39         w[layer][1][2] = -0.35451296;
40         w[layer][2][2] = 1.5276815;
41
42         b[layer][0] = 0.3902676;
43         b[layer][1] = -2.111224;
44         b[layer][2] = -1.7614105;

```

A. UDF Sample Code

```
1     row_w[layer] = 3;
2     column_w[layer] = 3;
3     row_l[layer] = 3;
4     column_l[layer] = 1;
5 }
6 else if (layer == 3)
7 {
8     w[layer][0][0] = -3.4542477;
9     w[layer][1][0] = -0.5867474;
10    w[layer][2][0] = 0.5891541;
11    w[layer][0][1] = -0.9601947;
12    w[layer][1][1] = -2.2188394;
13    w[layer][2][1] = -0.81540954;
14    w[layer][0][2] = -0.10619492;
15    w[layer][1][2] = 0.40564188;
16    w[layer][2][2] = -1.1841055;
17
18    b[layer][0] = 0.18154249;
19    b[layer][1] = 0.2338538;
20    b[layer][2] = 0.34972304;
21
22    row_w[layer] = 3;
23    column_w[layer] = 3;
24    row_l[layer] = 3;
25    column_l[layer] = 1;
26 }
27 else if (layer == 4)
28 {
29    w[layer][0][0] = -0.07111692;
30    w[layer][1][0] = -1.1830853;
31    w[layer][2][0] = -0.17939277;
32    w[layer][0][1] = -2.1680722;
33    w[layer][1][1] = 0.5477342;
34    w[layer][2][1] = -0.7915146;
35    w[layer][0][2] = 1.8235024;
36    w[layer][1][2] = 0.7305678;
37    w[layer][2][2] = 1.6919467;
38
39    b[layer][0] = -0.8187738;
40    b[layer][1] = -0.12444842;
41    b[layer][2] = -0.38089356;
```

Source Code A.3.: Thermal Conductivity Computations Part 3/4

```

1     row_w[layer] = 3;
2     column_w[layer] = 3;
3     row_l[layer] = 3;
4     column_l[layer] = 1;
5 }
6 else if (layer == 5)
7 {
8     w[layer][0][0] = 0.41977832;
9     w[layer][0][1] = 0.69990194;
10    w[layer][0][2] = 0.8189637;
11
12    b[layer][0] = 0.7062322;
13
14    row_w[layer] = 1;
15    column_w[layer] = 3;
16    row_l[layer] = 1;
17    column_l[layer] = 1;
18 }
19 for (int i = 0; i < row_w[layer]; i++)
20 {
21     for (int j = 0; j < column_l[layer - 1]; j++)
22     {
23         output[layer][i][j] = 0;
24         for (int k = 0; k < row_l[layer - 1]; k++)
25         {
26             output[layer][i][j] += w[layer][i][k] *
27                 output[layer - 1][k][j];
28         }
29         output[layer][i][j] += b[layer][i];
30         if (output[layer][i][j] <= 0.0)
31         {
32             output[layer][i][j] = exp(output[layer][i][j]) - 1.0;
33         }
34     }
35 }
36 }
37 // Denormalize the parameter before passing to the solver
38 return output[numLayers - 1][0][0] * k_mean;

```

Source Code A.4.: Thermal Conductivity Computations Part 4/4

Bibliography

- [1] Pierre Friedlingstein, Michael O'sullivan, Matthew W Jones, Robbie M Andrew, Luke Gregor, Judith Hauck, Corinne Le Quéré, Ingrid T Lujckx, Are Olsen, Glen P Peters, et al. Global carbon budget 2022. *Earth System Science Data Discussions*, 2022:1–159, 2022.
- [2] Bonnie J McBride. *Computer program for calculation of complex chemical equilibrium compositions and applications*, volume 2. NASA Lewis Research Center, 1996.
- [3] Ramses Snoeckx and Annemie Bogaerts. Plasma technology—a novel solution for CO₂ conversion? *Chemical Society Reviews*, 46(19):5805–5863, 2017.
- [4] Ulrich Kogelschatz. Dielectric-barrier discharges: their history, discharge physics, and industrial applications. *Plasma chemistry and plasma processing*, 23:1–46, 2003.
- [5] Alexander Fridman. *Plasma chemistry*. Cambridge university press, 2008.
- [6] A Fridman, A Chirokov, and A Gutsol. Non-thermal atmospheric pressure discharges. *Journal of Physics D: Applied Physics*, 38(2):R1, 2005.
- [7] Ansys. *Fluent user's guide*. Technical report, 2022.
- [8] Ante Hecimovic, Federico D'Isa, Emile Carbone, and Ursel Fantz. Enhancement of CO₂ conversion in microwave plasmas using a nozzle in the effluent. *Journal of CO₂ Utilization*, 57:101870, 2022.
- [9] F A D'Isa, E A D Carbone, A Hecimovic, and U Fantz. Performance analysis of a 2.45 GHz microwave plasma torch for CO₂ decomposition in gas swirl configuration. *Plasma Sources Science and Technology*, 29(10):105009, oct 2020.
- [10] Abraham J Wolf, FJJ Peeters, PWC Groen, WA Bongers, and MCM Van De Sanden. CO₂ conversion in nonuniform discharges: Disentangling dissociation and recombination mechanisms. *The Journal of Physical Chemistry C*, 124(31):16806–16819, 2020.
- [11] C K Kiefer, A Hecimovic, F A D'Isa, and U Fantz. Quenching microwave plasmas via gas injection into the effluent: Effects on the conversion of CO₂. SMuK, 2021.
- [12] C K Kiefer, A Hecimovic, A Meindl, D Rauner, and U Fantz. OES characterization of the microwave plasma torch in different configurations. Conference Mainz, 2022.

- [13] A Hecimovic, CK Kiefer, A Meindl, R Antunes, and U Fantz. Fast gas quenching of microwave plasma effluent for enhanced CO₂ conversion. *Journal of CO₂ Utilization*, 71:102473, 2023.
- [14] John D Anderson. McGraw-hill series in aeronautical and aerospace engineering. *Fundamentals of Aerodynamics, by*, pages 54–56, 2003.
- [15] George Keith Batchelor. *An introduction to fluid dynamics*. Cambridge university press, 1967.
- [16] Frank P Incropera, David P DeWitt, Theodore L Bergman, Adrienne S Lavine, et al. *Fundamentals of heat and mass transfer*, volume 6. Wiley New York, 1996.
- [17] Alexandre Joel Chorin. Numerical solution of the Navier-Stokes equations. *Mathematics of computation*, 22(104):745–762, 1968.
- [18] Ansys. Fluent theory guide. Technical report, 2022.
- [19] Suhas Patankar. *Numerical heat transfer and fluid flow*. Taylor & Francis, 2018.
- [20] C. Brochet, E. Carbone, and S Bastiani-Ceccotti. Fluid modelling of a microwave CO₂ plasma. Technical report, Max Planck Institute for Plasma Physics, Ecole Polytechnique Universite Paris-Saclay, Research internship report, 2016.
- [21] Sanford Gordon and Bonnie J McBride. Computer program for calculation of complex chemical equilibrium compositions and applications. part 1: Analysis. Technical report, 1994.
- [22] Sanford Gordon, B McBride, and Frank J Zeleznik. Computer program for calculation of complex chemical equilibrium compositions and applications. supplement 1: Transport properties. Technical report, 1984.
- [23] James N Butler and Richard S Brokaw. Thermal conductivity of gas mixtures in chemical equilibrium. *The Journal of Chemical Physics*, 26(6):1636–1643, 1957.
- [24] Charles R Wilke. A viscosity equation for gas mixtures. *The journal of chemical physics*, 18(4):517–519, 1950.
- [25] Christopher M Bishop and Nasser M Nasrabadi. *Pattern recognition and machine learning*, volume 4. Springer, 2006.
- [26] François Chollet et al. Keras. <https://keras.io>, 2015.
- [27] Diederik P Kingma and Jimmy Ba. Adam: A method for stochastic optimization. *arXiv preprint arXiv:1412.6980*, 2014.
- [28] Frank M White. *Fluid mechanics*. New York, 1990.

- [29] Pierre Sagaut and Yu-Tai Lee. Large eddy simulation for incompressible flows: An introduction. scientific computation series. *Appl. Mech. Rev.*, 55(6):B115–B116, 2002.
- [30] David C Wilcox et al. *Turbulence modeling for CFD*, volume 2. DCW industries La Canada, CA, 1998.
- [31] Zheng Yang, Xu Cheng, Xinghua Zheng, and Haisheng Chen. Reynolds-averaged Navier-Stokes equations describing turbulent flow and heat transfer behavior for supercritical fluid. *Journal of Thermal Science*, 30:191–200, 2021.
- [32] J Hinze. Turbulence 2nd edition. *MacGraw Hill, New-York*, 1975.
- [33] W Peter Jones and Brian Edward Launder. The prediction of laminarization with a two-equation model of turbulence. *International journal of heat and mass transfer*, 15(2):301–314, 1972.
- [34] David C Wilcox. Reassessment of the scale-determining equation for advanced turbulence models. *AIAA journal*, 26(11):1299–1310, 1988.
- [35] Kemal Hanjalić and Brian E Launder. A reynolds stress model of turbulence and its application to thin shear flows. *Journal of fluid Mechanics*, 52(4):609–638, 1972.
- [36] Victor Yakhot and Steven A Orszag. Renormalization group analysis of turbulence. I. basic theory. *Journal of scientific computing*, 1(1):3–51, 1986.
- [37] Florian R Menter. Two-equation eddy-viscosity turbulence models for engineering applications. *AIAA journal*, 32(8):1598–1605, 1994.
- [38] Henk Kaarle Versteeg and Weeratunge Malalasekera. *An introduction to computational fluid dynamics: the finite volume method*. Pearson education, 2007.
- [39] Stephen B Pope. *Turbulent flows*. Cambridge university press, 2000.
- [40] Tsan-Hsing Shih, William W Liou, Aamir Shabbir, Zhigang Yang, and Jiang Zhu. A new k- ϵ eddy viscosity model for high reynolds number turbulent flows. *Computers & fluids*, 24(3):227–238, 1995.
- [41] Ashwani K Gupta, David G Lilley, and Nick Syred. *Swirl flows*. Tunbridge Wells, 1984.